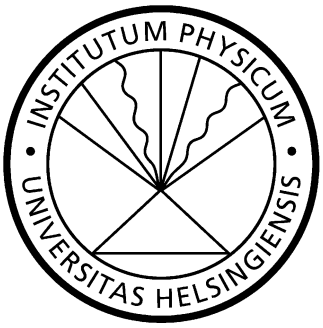

Master's thesis
Physics

Application of PIXE for the elemental analysis of coins

David Agaian

2020

Supervisors: Kenichiro Mizohata & Pasi Jalkanen

Reviewers: Jyrki Räisänen & Kenichiro Mizohata

UNIVERSITY OF HELSINKI
DEPARTMENT OF PHYSICS

PL 64 (Gustaf Hällströmin katu 2)
00014 Helsingin yliopisto

HELSINGIN YLIOPISTO — HELSINGFORS UNIVERSITET — UNIVERSITY OF HELSINKI

Tiedekunta – Fakultet – Faculty	Laitos – Institution – Department
Faculty of Science	Department of Physics

Tekijä – Författare – Author
David Agaian

Työn nimi – Arbetets titel – Title
Application of PIXE for the elemental analysis of coins

Työn laji – Arbetets art – Level	Aika – Datum – Month and year	Sivumäärä – Sidoantal – Number of pages
Master's thesis	November 2020	69

Tiivistelmä – Referat – Abstract
Particle Induced X-ray Emission (PIXE) is a nondestructive Ion Beam Analysis (IBA) technique that can be used for identifying elements in a sample. In PIXE, the radiation emitted by electron state changes is measured, after which emissions are recorded as spectral peaks. Each element is then identified based on its unique spectral peak.

PIXE analysis has been carried out using a 3 MeV proton beam generated with the aid of TAMIA 5 MV EGP-10-II tandem accelerator of the Department of Physics, University of Helsinki, at the Helsinki Accelerator Laboratory in Kumpula.

The external PIXE measurement setup in the accelerator laboratory has been prepared to study nine coins from 18th to 20th centuries and from different countries (Russia, USSR, Romania, France, and Portugal). The coins have been irradiated in the external PIXE setup, in which x-rays have been then detected by an x-ray detector. Two different detectors have been employed in the measurements: a KETEK AXAS-D Silicon Drift Detector (SDD) for detecting x-rays of every coin, and a Canberra GUL0110 Ultra-Low Energy Germanium (Ultra-LEGe) detector for detecting x-rays of silver coins.

After PIXE spectra have been obtained, PyMCA software has been used for the elemental analysis of the data. In the present study, various elements have been found from the measured PIXE spectra.

In silver coins, the following 10 elements have been specified: Ag, Cu, As, Pb, Fe, Sb, Ni, Zn, Sn and Bi.

In nickel plated steel coin observed elements are Fe, Ni, Co, and Cu.

Copper-zinc-nickel alloy coins have been found to consist of Cu, Zn, Ni, Fe, and Mn.

Copper-nickel alloy coins have been investigated to be made of Cu, Ni, Fe, and Mn.

This study verifies that the external PIXE technique can be utilized as a practical tool to identify elements in metallurgical samples.

Avainsanat – Nyckelord – Keywords
PIXE, IBA, beam exit window, SDD, Ultra-LEGe, MCA, PyMCA, elemental analysis

Säilytyspaikka – Förvaringställe – Where deposited
HELDA - Digital Repository of the University of Helsinki

Muita tietoja – Övriga uppgifter – Additional information

CONTENTS

1. INTRODUCTION

Particle induced x-ray emission (PIXE) is an ion beam analysis (IBA) technique which provides a nondestructive analytical method for identifying elements simultaneously in a sample. Moreover, PIXE is rather sensitive and rapid multi-elemental analysis with rather short measuring time and can be used for qualitative as well as quantitative research. Sample preparation procedures for PIXE are generally simple. The PIXE technique is utilized in numerous applications and in different research fields like materials science, archeology, environmental science, geology, biology etc [1-3].

The aim of the research and this thesis is to introduce the PIXE technique as a practical tool to identify elements in coins of different centuries. The application of scientific methods as PIXE to analyze coins can be specified in the following three areas: analysis of alloys, determination of provenance of the metal and technological studies. From the perspective of numismatics, the application of PIXE method provides valuable information of coins, for instance in changes of material technologies, economic conditions, political aspects, monetary theory, and art of coin design [4]. In addition, as a nondestructive technique PIXE is beneficial for analysis of ancient and valuable coins because it does not do any damage to the sample during the ion beam exposure.

1.1 Brief history of PIXE

In 1895, a German physics professor Wilhelm Röntgen [5] discovered x-rays while testing whether cathode rays could pass through glass. For this outstanding discovery he was awarded the first Nobel Prize in physics in 1901. X-rays are a form of electromagnetic radiation with a

very short wavelength. Throughout the years x-rays have gained great importance in wide range of applications in many fields of research and modern life.

In 1912, James Chadwick [6] showed that alpha particles from radioactive source can give rise to x-ray emission. However, due to too low signal and too low beam intensity this process was not useful for analytical purposes or practical applications until the development of particle accelerators for nuclear physics research.

As a phenomenon x-ray emission gained a lot of interest among physicists. Furthermore, a common appearance of x-rays as a background in nuclear physics experiments led to more specific theoretical and experimental research. The rapidly growing interest in this field required the improvement of experimental setup. In the 1950s, accelerators started to be used in the nuclear physics research.

The 1960s was a decade of significant progress in the nuclear detector technology. Wavelength-dispersive x-ray spectroscopy (WDS), which was at that point in time the most used detection method, got a great competitor of energy-dispersive x-ray spectroscopy (EDS) which started to utilize lithium-drifted silicon detectors, or shortly Si(Li) detectors. In comparison with EDS, WDS could detect one x-ray line at a time only, while EDS with Si(Li) detector and multichannel pulse-height analysis were capable to detect all the x-ray lines simultaneously.

The knowledge of cross sections as a function of particle energy and atomic number to produce x-rays as well as the possibility to use heavy charged particles allowed the development of multi-elemental analysis. In 1970, the first international conference on “PIXE and its applications” was organized, where PIXE was first introduced by Sven Johansson et al. [7] at the Lund Institute of Technology, Sweden. Johansson and his colleagues showed that using MeV protons with high resolution Si(Li) detector, it was possible to carry out multi-elemental and nondestructive analysis of trace elements with a good resolution at 10^{-12}g level. This ion

beam technique rapidly gained a lot of interest among physicists and started to be applied in many nuclear physics laboratories. By the 1980s, most of the technologies which utilized PIXE analysis were completed.

Starting from the year 1970 till this day, many international PIXE conferences have been organized, where the technical improvements and the applications of PIXE in several scientific fields have been introduced.

2. THEORY

PIXE is based on the detection of characteristic x-rays. For heavy elements, the probability of the emission of x-rays (de-excitation) is close to 1, but for light elements it is only few percent [8]. To determine the probability of characteristic x-ray production in elemental analysis by PIXE technique, there are fundamental parameters called ionization and x-ray production cross sections. In addition, the best theory for calculating inner shell ionization cross sections in PIXE method is introduced.

As continuous background is present in experiments, it is covered by discussing in more detail about the sources of radiative processes which contribute in experimental PIXE spectra. In addition, for ease of understanding the experimental data, a quantitative analysis of the experiment is discussed.

2.1 Characteristic x-rays

When target atom is bombarded with heavy charged particles (from protons to heavy ions, usually MeV protons in PIXE method) it gets excited. The collision of charged particles with the target atom ejects the innermost shell electrons of the atom and causes a vacancy in the atomic inner shell. The excited atom seeks to regain a stable energy state by filling the vacancy in the inner shell with outer shell electrons. When an electron makes transition between the atomic energy levels, the electron emits a certain amount of energy in form of radiation which is called characteristic x-ray. In Figure 1, an atom is bombarded with a proton causing an ejection of an electron, ionization of K-shell and emission of characteristic x-ray. This is the main principle of PIXE method to produce characteristic x-rays.

Occasionally an excited atom might de-excite by the emission of an electron, known as Auger electron. On that occasion, the energy is higher than the binding energy of the electron, the electron gets ejected from its shell, and the atom does not emit characteristic x-ray. The atomic de-excitation can still produce both characteristic x-rays and Auger electrons or either of the two.

In each element there is a unique set of energy levels which is determined by its protons and neutrons of the nucleus. Furthermore, atoms of a particular element have the same set of energy levels and because of that the element can be identified by characteristic x-rays.

If a certain amount of energy is applied to an atom, it can remove an electron from it. To be able to remove the electron from the atom it requires that the applied energy must be greater than the electron binding energy. The binding energies of the electrons go down as the further the electron shell is located from the nucleus. The emitted x-ray energy E_x which occurs when an electron makes a transition from an outer shell with electron binding energy E_o to inner shell with binding energy E_i which can be calculated with the equation

$$E_x = E_i - E_o \ . \tag{1}$$

The energy levels of the electrons in the atom determine x-ray spectrum. Figure 2 shows an energy level diagram and electron transitions which are allowed by the quantum-mechanical selection rules [9] in a medium-heavy element. The electron transitions to the K-shell which produce x-rays are called K x-rays. More specifically, if the electron which fills the vacancy in K-shell comes from the L_{III}-shell, the emitted x-ray is denoted $K_{\alpha 1}$, and when the transition is from L_{II}-shell, the emitted x-ray is indicated $K_{\alpha 2}$. If the K-shell electron vacancies are filled by the electrons which come from M_{III}-shell and from M_{II}-shell, the emitted x-rays denote $K_{\beta 1}$ and $K_{\beta 2}$. Some components, for example the K_α x-ray components $K_{\alpha 1}$ and $K_{\alpha 2}$, have approximately the same energy which cause that they appear as a single K_α peak in the spectrum. Usually, the effective detection of light and medium-heavy elements with atomic numbers greater than 20

and less than 50 can be obtained by K x-rays [10].

The vacancies created in the L-shell and filled by the outer M-shell electrons produce L x-rays are also presented in Figure 2 as the electron transitions. Generally, heavy elements with atomic number greater than 50 are identified by L x-rays [10].

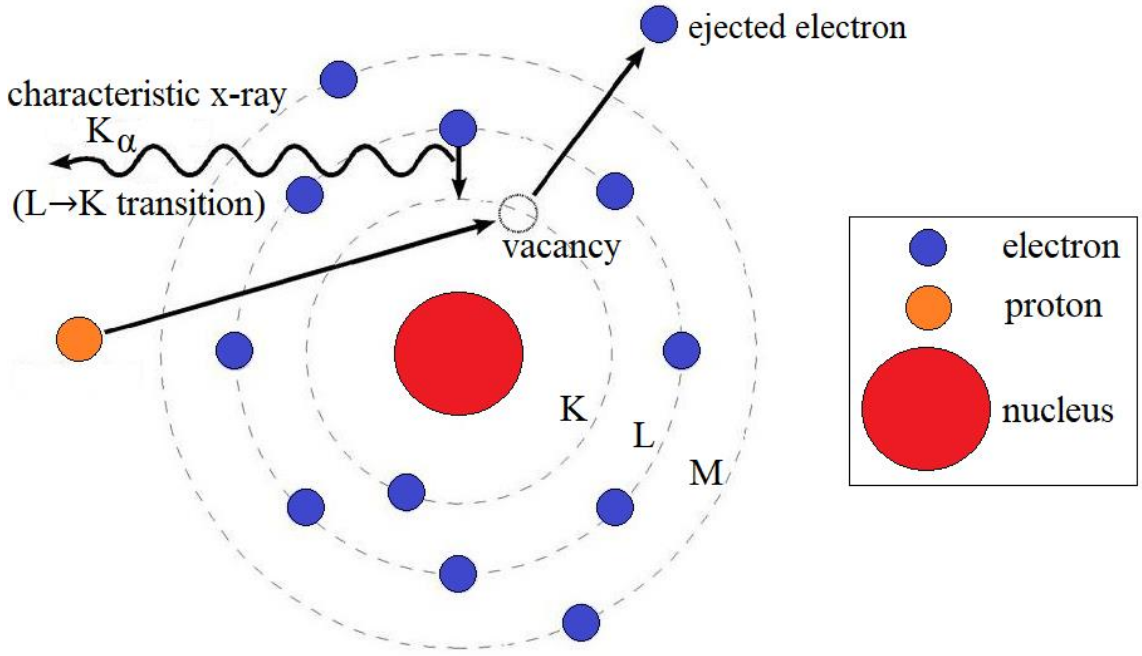

Figure 1: *Illustration of characteristic x-ray production in PIXE method.*

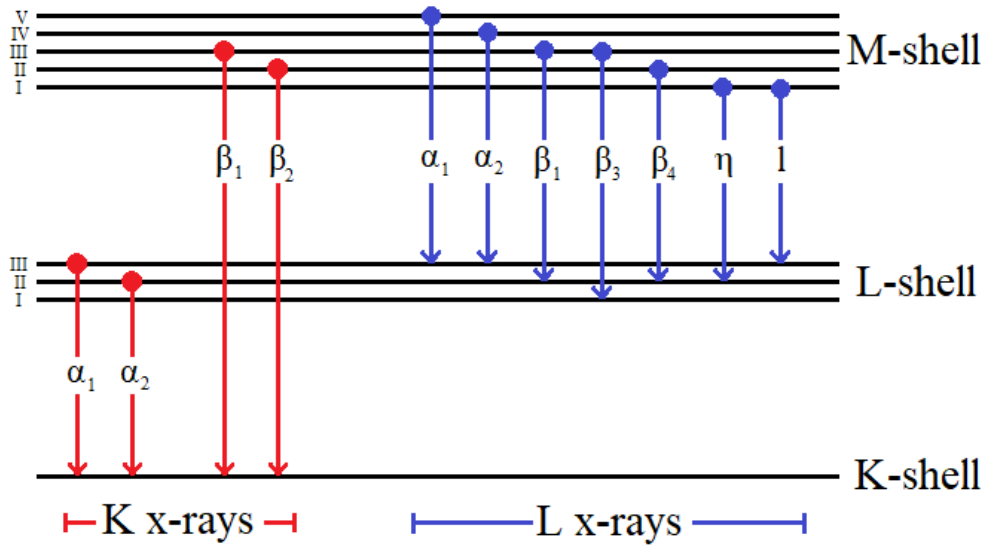

Figure 2: *Energy levels and electron transitions producing x-rays in medium-heavy element.*

2.2 Cross sections of x-ray production

The probability of x-ray production due to that a particular shell will be ionized by the incident charged particle is defined in terms of the x-ray production cross section. For example, the transitions to the K-shell from the L-shells and M-shells (presented in Figure 2) occur in PIXE spectrum as two different x-ray peaks, K_α and K_β, depending on from which shell the electrons make transition. We denote the transition probability of K_α x-rays as Γ_α^X, the transition probability of K_β x-rays as Γ_β^X, and the transition probability of Auger electrons as Γ^A. The emission ratio of x-ray ω, also known as fluorescence yield [11], is defined by the equation

$$\omega = \frac{\Gamma_\alpha^X + \Gamma_\beta^X}{\Gamma_\alpha^X + \Gamma_\beta^X + \Gamma^A} \ . \tag{2}$$

The total production cross sections of K_α and K_β x-rays are expressed by the equations

$$\sigma_{K_\alpha}^X = \frac{\Gamma_\alpha^X}{\Gamma_\alpha^X + \Gamma_\beta^X}\omega_K\sigma_K^i \quad \text{and} \quad \sigma_{K_\beta}^X = \frac{\Gamma_\beta^X}{\Gamma_\alpha^X + \Gamma_\beta^X}\omega_K\sigma_K^i \ , \tag{3}$$

where ω_K is K-shell fluorescence yield and σ_K^i is K-shell ionization cross section. [12] For K-shell vacancy production induced by a charged particle (E_p, Z_1) can be presented by the equation

$$\sigma_K = \frac{Z_1^2}{U_K^2} f(E_p, M_1, U_K) \ , \tag{4}$$

where Z_1 is the atomic number of the projectile, U_K is K-shell electron binding energy, E_p is the projectile energy, and M_1 is the projectile mass. The cross sections of L x-ray (L_α, L_β and L_γ) production can be presented by the same principle as in equations $(2) - (4)$.

2.2.1 Introduction of ECPSSR model

The knowledge of accurate ionization cross sections and then the total x-ray production cross sections is of great importance for the quantitative PIXE analysis. Generally, if there are

significant uncertainties such as noise in the experimental data of PIXE, it is necessary to utilize a convenient theoretical model to predict ionization cross sections and compare them to the results obtained from the experiment. The best theory for calculating inner shell ionization cross sections is energy coulombian perturbed stationary state relativistic theory, also known as ECPSSR model [13], which is based on plane wave Born approximation (PWBA) theory including various improvements which are formed on plausible physical considerations [14]. The ECPSSR theory is developed by Werner Brandt and Grzegorz Lapicki [15].

In the ECPSSR, E denotes the energy loss, C stands for Coulomb deflection of the projectile ion, PSS is the perturbed stationary state, and R describes relativistic nature of the electron of the target in inner shell. The theoretical ECPSSR ionization cross section is given by the equation

$$\sigma_{ECPSSR} = C_S(dq_{0_S})F_S(Z)\sigma_{PWBA}(m^R(\xi_S)\eta_S, \zeta_S\vartheta_S)\,, \qquad (5)$$

where $C_S(dq_{0_S})$ represents the Coulomb deflection factor [16], $F_S(Z)$ is the energy loss correction factor [15], $m^R(\xi_S)\eta_S$ and $\zeta_S\vartheta_S$ are the relativistic and the binding energy corrections [15], and σ_{PWBA} denotes the atomic ionization cross section obtained from the PWBA model [14].

The accuracy of K-shell ionization cross sections given by the ECPSSR theory is confirmed to be in general within 10% agreement to the experimental values [17]. In case of L-shell ionization cross sections, the ECPSSR model is in good agreement with the data when shell is induced by protons of energies above 2 MeV [18]. At low projectile velocities the deviations can be observed – the ECPSSR theory overpredicts experimental results [19].

2.3 Continuous background

PIXE spectra obtained from experimental data contain approximately Gaussian characteristic x-ray peaks with continuous background, mostly caused by electromagnetic radiation. Background underlies characteristic x-ray peaks and increases the statistical error of the experimental results. Most of the background radiation is due to the production of secondary electrons which occurs as a part of the excitation process. Thus, higher x-ray yields lead also to proportionately higher secondary electron production which cause bremsstrahlung within the target. There are three sources of radiative processes which explain well continuous background and contribute to a low energy PIXE spectrum: atomic bremsstrahlung (AB), secondary-electron bremsstrahlung (SEB), and quasi-free-electron bremsstrahlung (QFEB). There are also other sources causing continuous background to some extent, such as nuclear bremsstrahlung, Compton scattering, Rutherford scattering, cosmic rays, and environmental radiation [20].

It is important to be aware of the sources that might contribute to existence of continuous background in the experimental data to be able to minimize it. In addition, by collecting the continuous background data separately (without a target sample), it can be identified and subtracted from the PIXE spectrum. Most PIXE data analysis software offer a background modelling, where the background is predicted based on detected points which belong to it. Detected x-ray peaks are then separated from the background with an analytical function.

2.3.1 Atomic bremsstrahlung

Atomic bremsstrahlung is generated in collisions of a projectile and a target. The interaction between the projectile proton and an inner shell electron of the target leads to the excitation of the electron to a continuum state. During the de-excitation, the electron drops to a lower state

and emits photons with continuum spectra which are known as atomic bremsstrahlung. Emitted photons have continuum spectra because they come from different depths of the material which make them to lose varying amount of energy. Atomic bremsstrahlung cross section σ^{AB} can be defined from the equation of the PWBA theory and hydrogen-like wavefunction [21]:

$$\frac{d\sigma^{AB}}{d(\hbar\omega)} = \frac{8a_0^2\alpha^5}{\pi\hbar\omega} Z_p^2 \left(\frac{c}{v_p}\right)^2 \frac{\int_\omega^\infty \frac{dq}{q}}{v_p} \times \left\{1 - \left(\frac{\omega}{qv_p}\right)^2 + \left[\frac{3}{2}\left(\frac{\omega}{qv_p}\right)^2 - \frac{1}{2}\right] sin^2\,\theta_L\right\} \times \left|Z_p S(Z_T, q)\right|^2, \quad (6)$$

where a_0 denotes the Bohr atomic radius, α denotes the fine-structure constant, $\hbar\omega$ is the energy of photon, Z_p and Z_T are atomic numbers of the projectile and the target, c denotes the speed of light in vacuum, v_p is velocity of the projectile, θ_L stands for the photon emission angle with respect to the projectile direction, and $Z_p S(Z_T, q)$ is given in the literature [22].

2.3.2 Secondary electron bremsstrahlung

After the electron of the target atom is ejected by the projectile proton, the electron interacts with the Coulomb field of the target's nucleus during the time it passes through the material of the target. The electron scatters and loses energy by emission of secondary electron bremsstrahlung. When the electron ejection cross sections obtained from binary encounter approximation theory, electron bremsstrahlung of PWBA equation and the energy loss from Bethe equation are combined, the secondary electron bremsstrahlung cross section σ^{SEB} can be expressed by the following equation [23]:

$$\frac{d\sigma^{SEB}}{d(\hbar\omega_L)} = \frac{1}{2\pi} Z_p^2 \left(\frac{e^2}{\hbar c}\right)^5 a_0^2 Z_T \frac{m_e c^2}{(\hbar\omega)^2} (C_1 + C_2 sin^2\theta_L)\,, \quad (7)$$

where $\hbar\omega$ and $\hbar\omega_L$ denote energies of photon before and after scattering, Z_p and Z_T represent atomic numbers of the projectile and the target, $\hbar$ is the Planck's constant, c is the speed of light in vacuum, a_0 is the Bohr atomic radius, m_e is mass of the electron, θ_L stands for the photon

emission angle, and both C_1 and C_2 are given in the literature [24].

Secondary electron bremsstrahlung can be characterized by the equation

$$T_m = 2m_e V_P^2 \,, \tag{8}$$

where T_m is the maximum energy of the projectile capable of transferring to a free electron at rest, m_e stands for mass of the electron, and V_p denotes velocity of the projectile [25]. When the energy is higher than T_m, the intensity of SEB decreases rapidly due to higher number of free and outer shell electrons compared with the number of inner shell electrons.

2.3.3 Quasi-free electron bremsstrahlung

Quasi-free electron bremsstrahlung occurs when the velocity of the electron in the atom is significantly slower than the velocity of the projectile. During the scattering of the electron in the projectile's Coulomb field, QFEB is generated. Quasi-free electron bremsstrahlung cross section σ^{QFEB} can be defined from the equation [24]

$$\frac{d\sigma^{QFEB}}{d\Omega d(\hbar\omega)} = \frac{N_\tau}{\pi} Z_p^2 \left(\frac{e^2}{\hbar c}\right)^5 a_0^2 \frac{m_e c^2}{T_r \hbar\omega} \times [sin^2\,\theta + \frac{1}{4}(1+p^2)(3\,cos^2\,\theta - 1)\,ln\left(\frac{1+p}{1-p}\right) - \frac{1}{2}p(3\,cos^2\,\theta - 1)] \,, \tag{9}$$

where N_τ represents the number of electrons of the target atom, Z_P is the atomic number of the projectile, $\hbar$ is the Planck's constant, c is the speed of light in vacuum, m_e is mass of the electron, T_r denotes relative kinetic energy, $\hbar\omega$ is the energy of photon, Ω denotes the solid angle, θ represents the scattering angle, and $p^2 = 1 - \frac{\hbar\omega}{T_r}$.

Relative kinetic energy T_r characterizes quasi-free electron bremsstrahlung by the following equation [26]:

$$T_r = \frac{m_e E_P}{M_P} \,, \tag{10}$$

where m_e is mass of the electron, E_P stands for the energy of the projectile, and M_P denotes mass of the projectile.

2.4 Quantitative analysis

When appropriate parameters are used with the experimental data, it is possible to analyze the elemental composition of the target [27]. The elemental composition of the sample can be defined from obtained PIXE spectra by using the formula

$$dN = A(s)n(s)\sigma\omega k\Omega T\varepsilon dS\ , \tag{11}$$

where dN is the number of counts which are coming from the number of $A(s)$ atoms, $n(s)$ stands for the number of protons passing through the surface element dS, σ denotes cross section for ionization, ω is the fluorescent yield, k is the probability for relative transition for the x-ray transition used in experiments, Ω represents the solid angle, T stands for transmission through irradiation chamber window, and ε is efficiency of the detector [28].

The total number of counts in the peak can be obtained by integrating the formula (11). By taking the beam density distribution as a uniform and $n(s)$ as a constant, and integrating $A(s)$ over the whole surface dS, the following formula is obtained:

$$N = An\sigma\omega k\Omega t\varepsilon\ , \tag{12}$$

where N represents the total number of counts in specific peak, and A stands for the total number of atoms of specific element in the sample. The values of N for each peak are obtained directly from the experimental data. Measured PIXE spectra without an energy calibration are presented on a logarithmic scale in **Appendix A: Raw spectral data**.

3. EXPERIMENT

The experiment has been carried out at the Helsinki Accelerator Laboratory of the Department of Physics, University of Helsinki, Kumpula. The layout of the accelerator laboratory and the facilities with ion beams [29] are presented in Figure 3. Irradiation process was performed by 5 MV tandem accelerator which generated 3 MeV protons for the PIXE experiment. This experimental part will cover the fundamental parts of the beam transmission path including ion source, accelerator, and beamline. In addition, an external PIXE setup used for the experiment is covered in more detail. Furthermore, samples and reference materials used in the experiment, preparation of these samples for the experiment, as well as processing of experimental data is discussed.

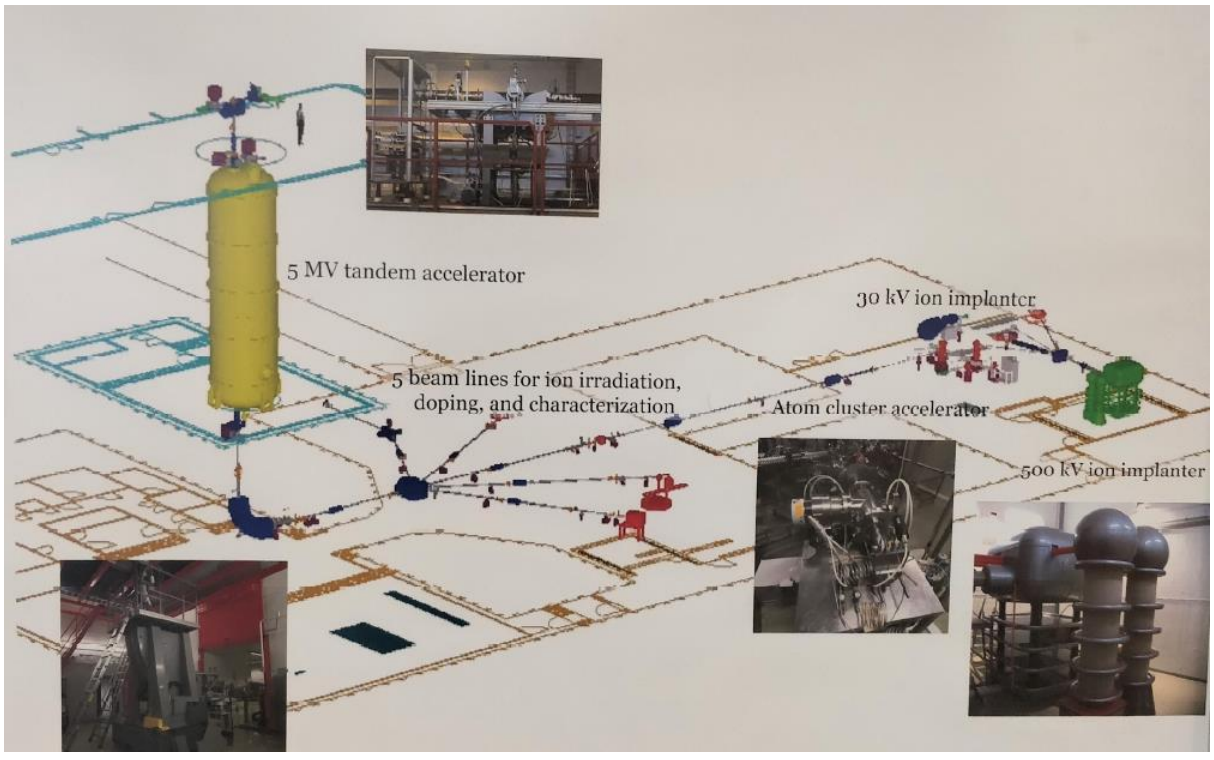

Figure 3: *3D layout of the accelerator laboratory.*

3.1 Beam transmission path

Figure 4 shows the beam transmission path with all parts from ion source throughout the accelerator to the beamline. Exact locations of the three parts are illustrated in the layout of the accelerator laboratory.

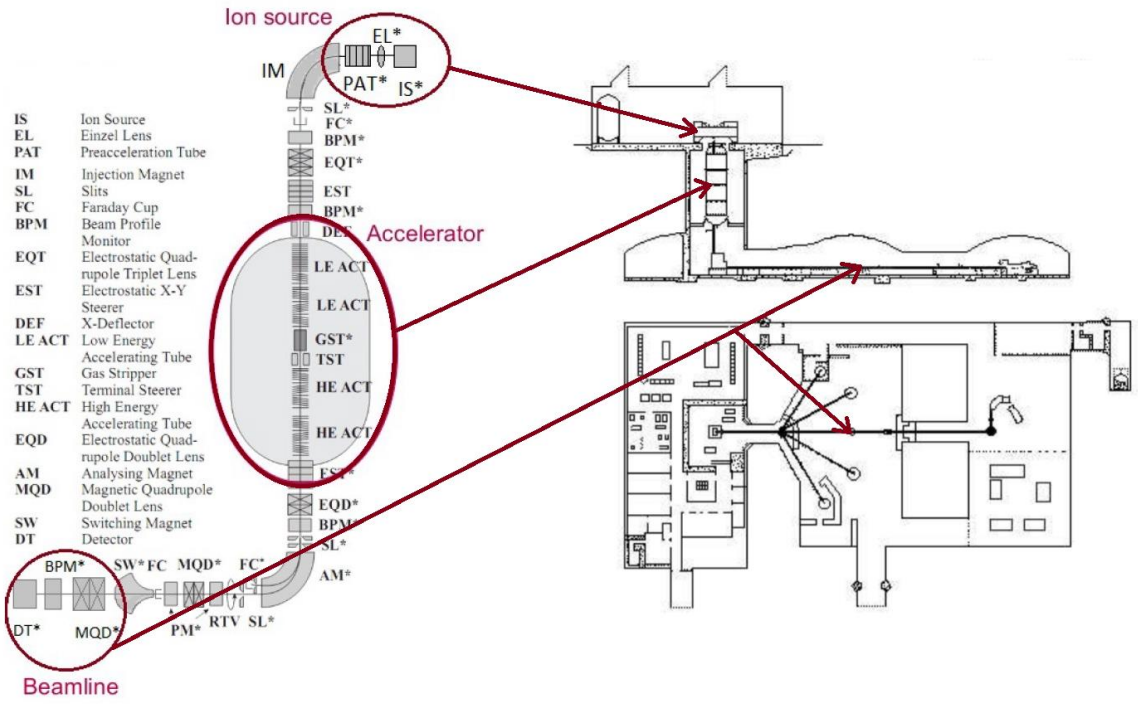

Figure 4: *Beam transmission path in 2D accelerator laboratory layout.*

3.1.1 Ion source

In the experiment, a cesium sputtering ion source has been used. It is a negative ion source which is used for producing ion beams. The sputtering process occurs in an enclosed area in the ion source which has a cooled cathode and a heated ionized surface. Cesium vapor which is produced in the oven flows into the enclosed area and gets ionized for the most part by the heated surface. Some of cesium gets condensed on the front of the cathode. Through the formed

condensed cesium layer on the surface of the cold cathode, the ionized cesium sputters particles and produces negatively charged ions [30].

3.1.2 Accelerator

Negative ions generated in the ion source are directed through the injection magnet to the TAMIA 5 MV EGP-10-II tandem accelerator. This accelerator uses a generator and two-stage tandem acceleration to produce protons of desired energy.

In the generator there is an insulated conveyor belt that transports charge to a terminal. These charges are generated through a high-voltage DC supply and then collected in the inside of the terminal and transferred to external surface [31].

For the first stage of a tandem accelerator, the negative ions which are generated in the ion source are accelerated towards the positive high-voltage terminal. This terminal has a gas stripper in the middle of the accelerator. There the negative ions are stripped off from electrons trough gas volume to become positively charged ions. The positive ions are then accelerated as they move from the positive potential on the center of electrode back to the ground [32].

When the electrons of negative ions are stripped off, the second stage of acceleration begins. The positive ions, now repelled by the positive terminal, are further accelerated through the tube. At the output end of the accelerator, protons are magnetically separated from other particles and directed further to the beamline [33].

3.1.3 Beamline

The proton beam obtained from the accelerator moves further to the beamline through the analyzing magnets. The protons will then go through the collimator to keep the beam in focus.

To measure beam current there is a beam profile monitor (BPM) which is in vacuum at the end of the beamline. BPM is placed before the exit window after which the proton beam enters the laboratory atmosphere.

3.2 External PIXE setup

An external PIXE setup has many advantages over an internal PIXE which is usually performed in a vacuum environment [34]. Great benefit of external PIXE is the possibility of measurement at atmospheric pressure. This makes sample preparation and handling significantly easier and speeds up switching between samples. In addition, bringing the proton beam to air reduces heating on the surface of the sample on the beam target spot, so there is no danger to any sample damage. Another great benefit of external PIXE is that the sample charging is also avoided.

A compact external PIXE setup which is presented in Figure 5 has been used to detect x-rays of nine coins. Each coin has been exposed to 3 MeV proton beam for 400-600 seconds in experimental box which is dark inside to prevent external light contamination and minimize noisy data. Before x-ray measurements of each coin, background and then standard reference materials of known compositions have been measured. Before each data collection set, lights of the room have been switched off. A video camera and an external monitor have been used as to set the target spot of the beam on the target sample.

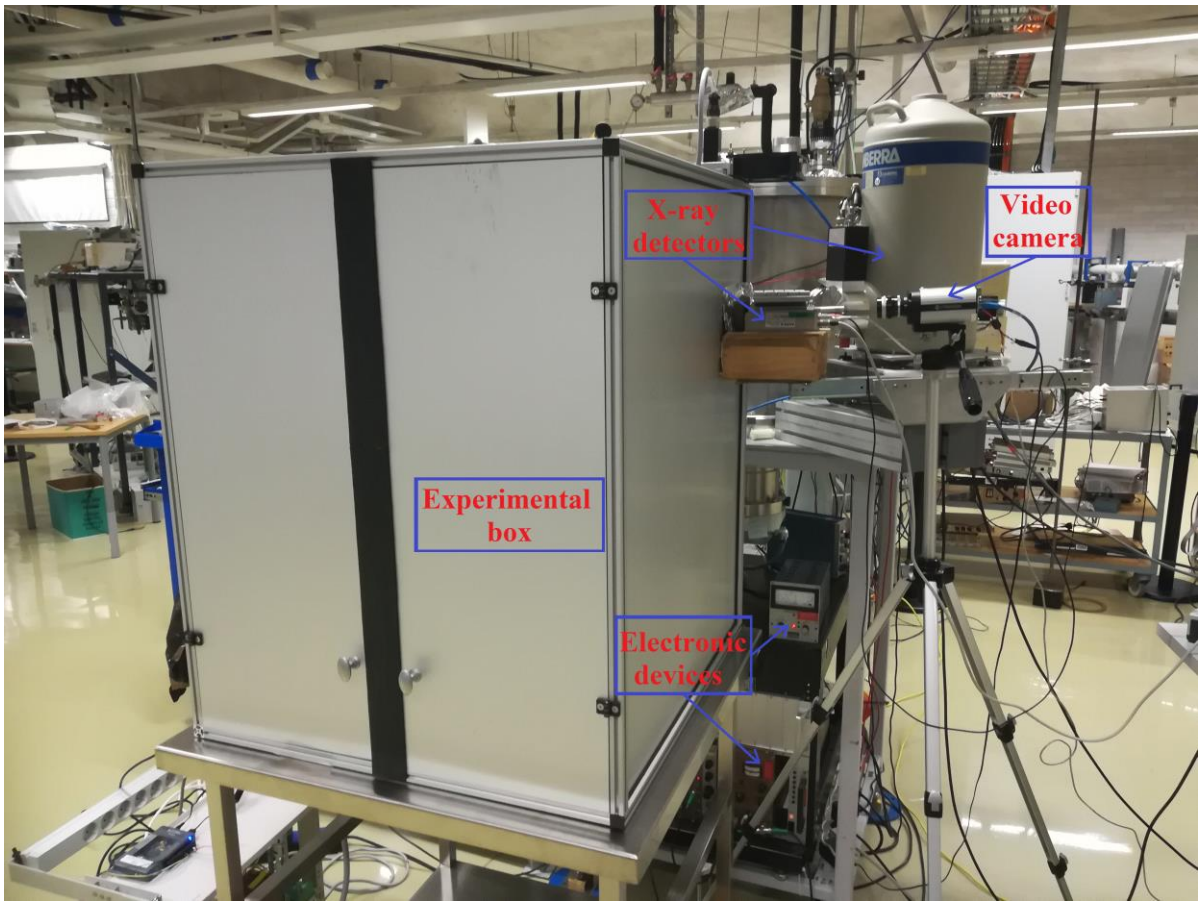

Figure 5: *Snapshot of external PIXE setup.*

3.2.1 Beam exit window

Figure 6 presents a general layout of external PIXE beam configuration including profilometer which measures current, fast shutoff valve for vacuum protection, vacuum meter as well as the closeup figure of the parts which are inside the experimental box: beam exit window, sample holder and x-ray detector [34]. The proton beam travels from vacuum to the laboratory atmosphere through a beam exit window into the experimental box. Only one thin membrane of silicon nitride (Si_3N_4) has been used as the exit window. In addition, there has been a thin beam exit foil which withstands a pressure difference due to it separates the vacuum from the laboratory atmosphere. Beam exit foils are commonly made of polymers such as Kapton films,

but there are also other suitable options, for instance, aluminized Mylar, nickel, and zirconium foils [35]. Silicon nitride has a great advantage over the other materials because they cannot be as thin and durable as Si_3N_4.

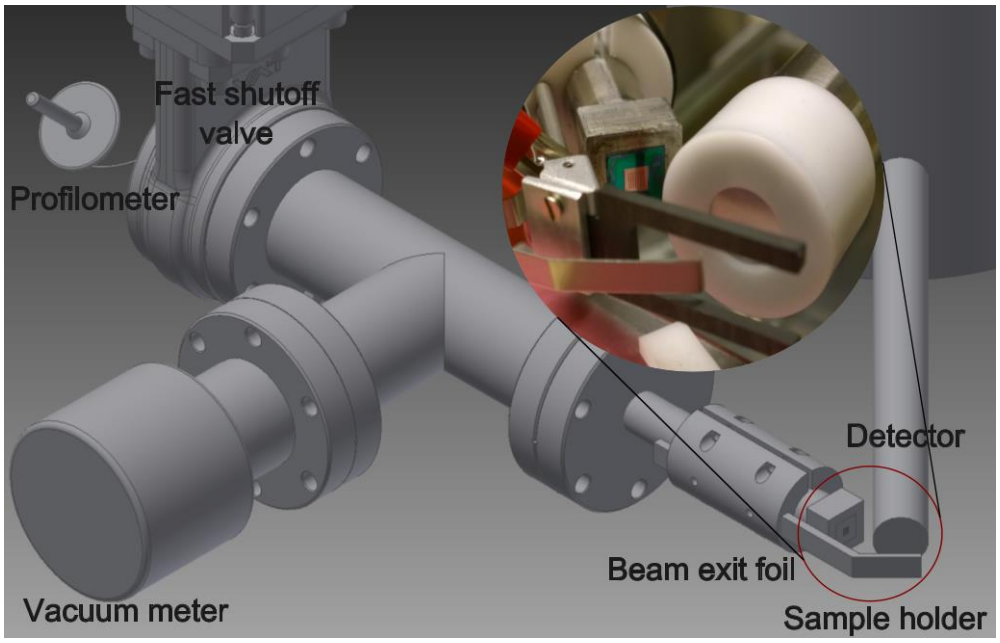

Figure 6: *Layout of external PIXE beam configuration.* [34]

3.2.2 Beam-sample-detector geometry

Changes in the beam-sample-detector geometry affect measurement results. The geometry of the measurements with the same detector must be kept the same to minimize systematic errors in intensity measurement. Moreover, each sample must be inserted and removed carefully from the sample holder to not to change the measurement geometry.

The measurements have been separately performed by two different x-ray detectors which are presented in Figure 7. In the first measurements of the coins, the x-rays of each coin have been detected by a KETEK AXAS-D Silicon Drift Detector (SDD), with no absorber foil. The measurement geometry has been chosen so that from perspective of the sample holder there is

an angle of 90° between the beam exit window and the SDD. For every measurement with the SDD, each coin has been placed inside the experimental box to the sample holder and kept the same position at 45° angle from the normal to the beam exit window and to the detector. The genuine geometry of the external PIXE setup inside the experimental box is presented in Figure 8.

After the first measurements, the SDD has been moved further from the sample holder and the other detector closer to it. The detection of x-rays in the second measurements has been performed with a Canberra GUL0110 Ultra-Low Energy Germanium (Ultra-LEGe) detector. Six thin aluminum foils and one Kapton film have been used as filters to absorb unwanted low energy x-rays of secondary electrons. The filters have been placed inside the white part (presented in Figure 8), so that the filters are in front of the entrance window of the detector. The measurements with Ultra-LEGe detector has been performed geometrically at an angle of 60° respectively, where both the incident and the exit angles have been equal to 30°. Four coins have been observed to be composed of silver, and their experimental data have been detected by the Ultra-LEGe detector.

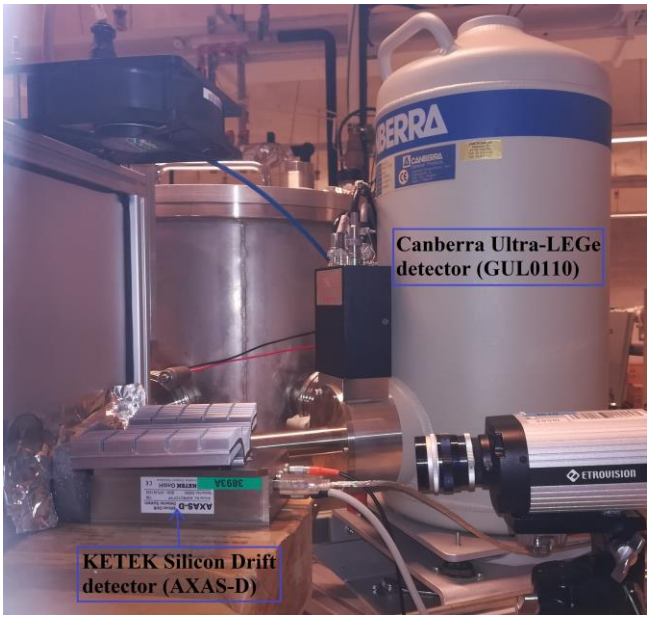

Figure 7: *X-ray detectors.*

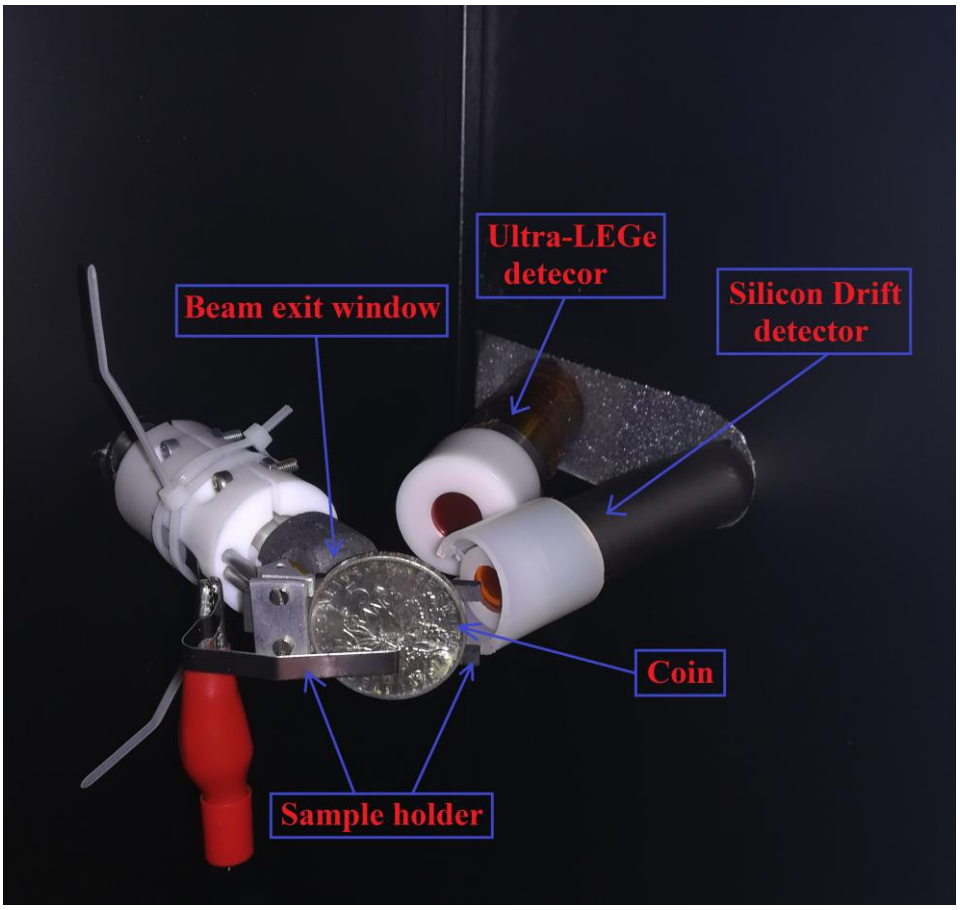

Figure 8: *Geometry of the external PIXE setup inside the experimental box.*

3.2.3 X-ray detectors and electronic devices of the measurements

Figure 9 presents the construction and operation of the silicon drift detector. The sensor of the detector consists of 30 mm² SDD chip collimated to 20 mm² active area [36]. X-rays enter the detector through the 8 μm beryllium window and the cathode. On the opposite side of the x-ray entrance inside the detector, there is a small anode contact in the middle, which is surrounded by several concentric drift electrodes. Through the x-ray ionization process, the detector converts an x-ray of a particular energy into an electric charge of proportional size. The SDD utilizes a field gradient which is applied by ring electrodes on its back surface. This enables at the anode to collect the charge liberated by each detected x-ray. The SDD operates at a few tens

of degrees below zero and must be cooled by thermoelectric Peltier elements which transfer heat from the inner part of the detector to heatsink and then to air [37].

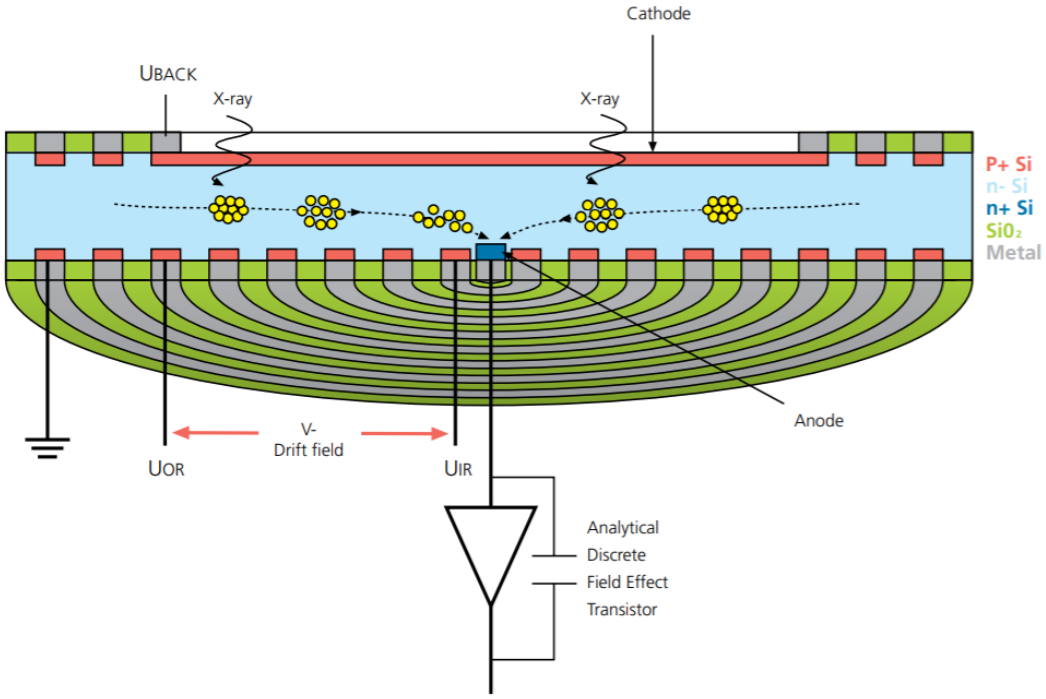

Figure 9: *Construction and operation of the silicon drift detector.* [37]

Canberra GUL0110 Ultra-LEGe detector, which has been used in the data collection of silver coins, has a 0.025 mm beryllium window with an active area of 100 mm² and thickness of 10 mm. An illustration of the entrance of the Ultra-LEGe detector is presented in Figure 10. This ultra-low energy germanium detector covers a wider range of energies – from 300 eV to 300 keV. The detector manufacturer informs that the resolution at 5.9 keV is less than 150 eV (FWHM) [38]. One of the major advantages of the Ultra-LEGe detector is that it has a low capacitance. This permits it to maintain a good energy resolution performance even at very short shaping times. Ultra-LEGe detector has a P-I-N structure in which the intrinsic region is sensitive to x-rays. An electric field extends across the intrinsic or depleted region when it is under reverse bias. When x-rays interact with the material within the depleted volume of a detector, charge carriers (holes and electrons) of the semiconductor material are produced and

then swept by the electric field to the P and N electrodes. Germanium has a relatively low band gap because of significantly weak bonding between its atoms. This leads to thermal generation of charge carriers in the Ultra-LEGe detector. The detector must be cooled with liquid nitrogen (LN_2), with which a dewar of the detector has been filled eight hours prior to measurements. Cooling the detector reduces unwanted noise and improves the energy resolution. In addition, the sensitive surfaces of the detector are well protected from different type of contaminants [39].

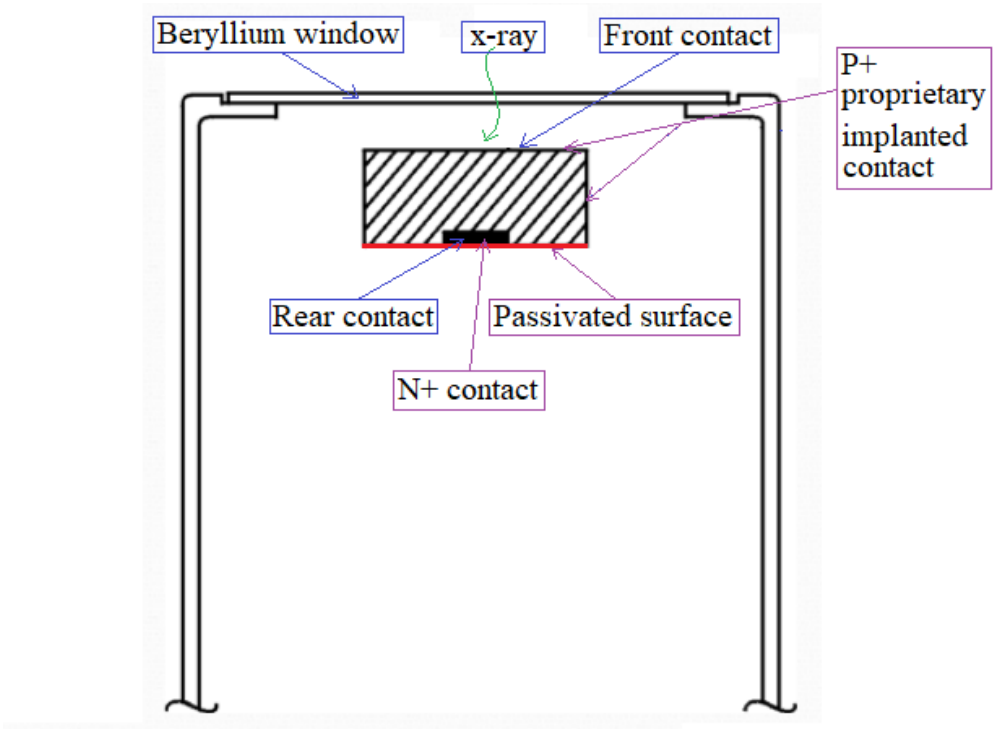

Figure 10: *Entrance of the Ultra-LEGe detector.*

In Figure 11 radiation detection efficiencies of silicon drift and ultra-low energy germanium detectors are compared. SDD is particularly suitable for detecting lighter elements at lower radiation energies, whereas Ultra-LEGe detector performs better efficiency results at higher radiation energies and heavier elements.

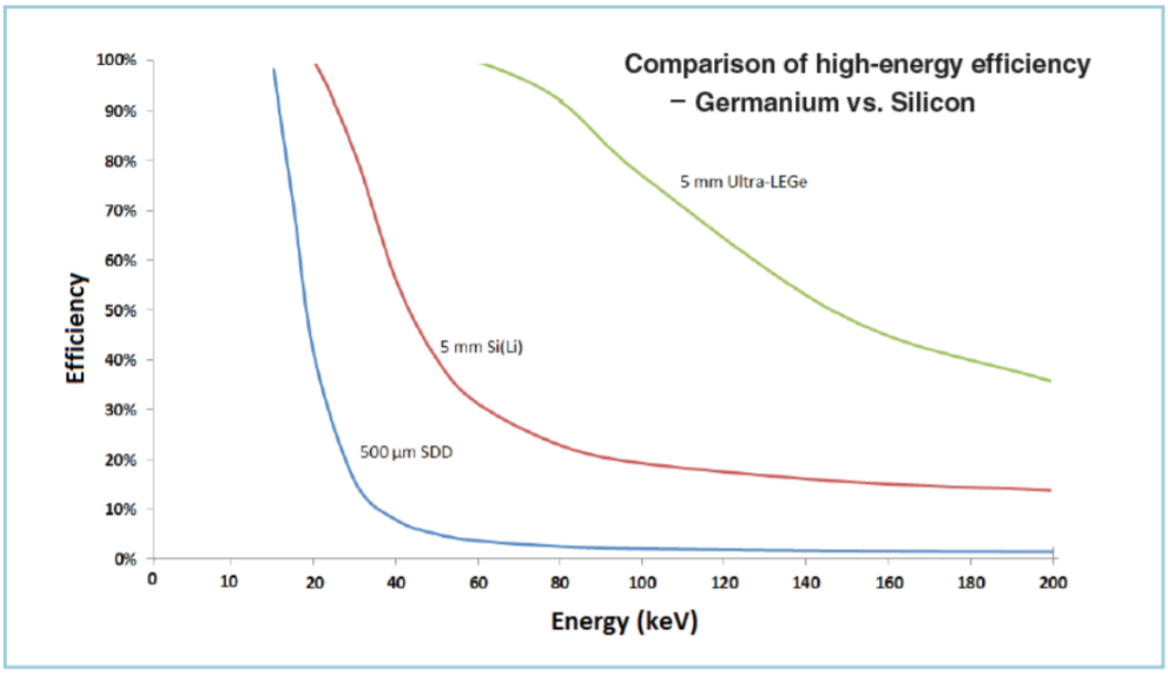

Figure 11: *Comparison of detection efficiency among silicon and germanium detectors.* [40]

Electronic devices after the detector take care of pulse collection and transfer to displayed spectrums. A schematic illustration of used electronic devices and their connections is presented in Figure 12. As the output of the detector is a charge pulse and is proportional to the energy deposited in the detector by the incoming x-ray, it is converted into a voltage pulse by an integral charge-sensitive preamplifier. The preamplifier is connected to a high voltage power supply with coaxial cables and to linear amplifier which carries out the conversion of the signals. The amplifier output goes to the analog-to-digital converter (ADC) and after that to the input of Multi-Channel Analyzer (MCA) which distributes different received amplitudes. The output of MCA is connected to the computer from which the experimental data can be visualized as an energy spectrum. The MCA program of the computer enables taking data of the total number of counts under the peaks as well as the measurement time. Experimental data obtained from the measurements have been collected in the control room which is presented in Figure 13.

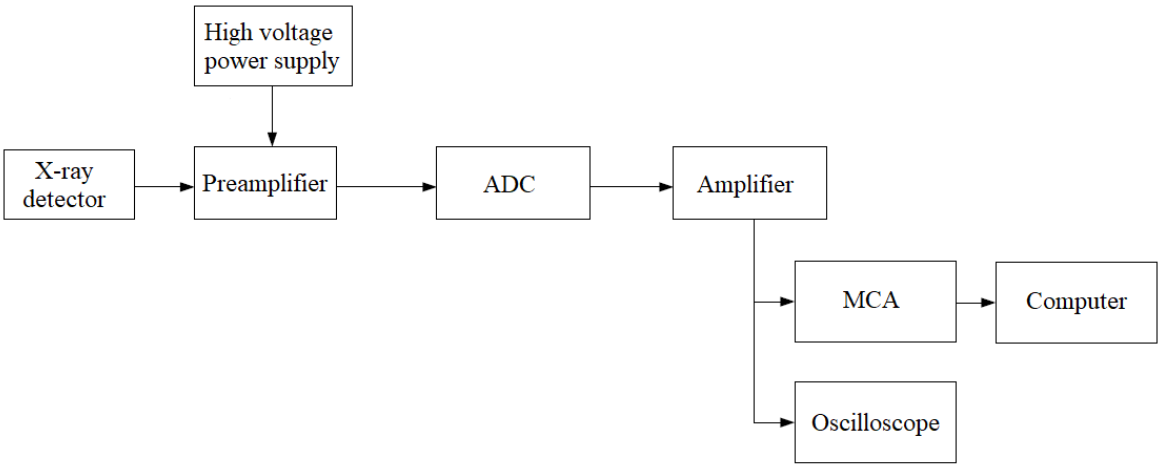

Figure 12: *Schematic illustration of electronic device connections of the experimental setup.*

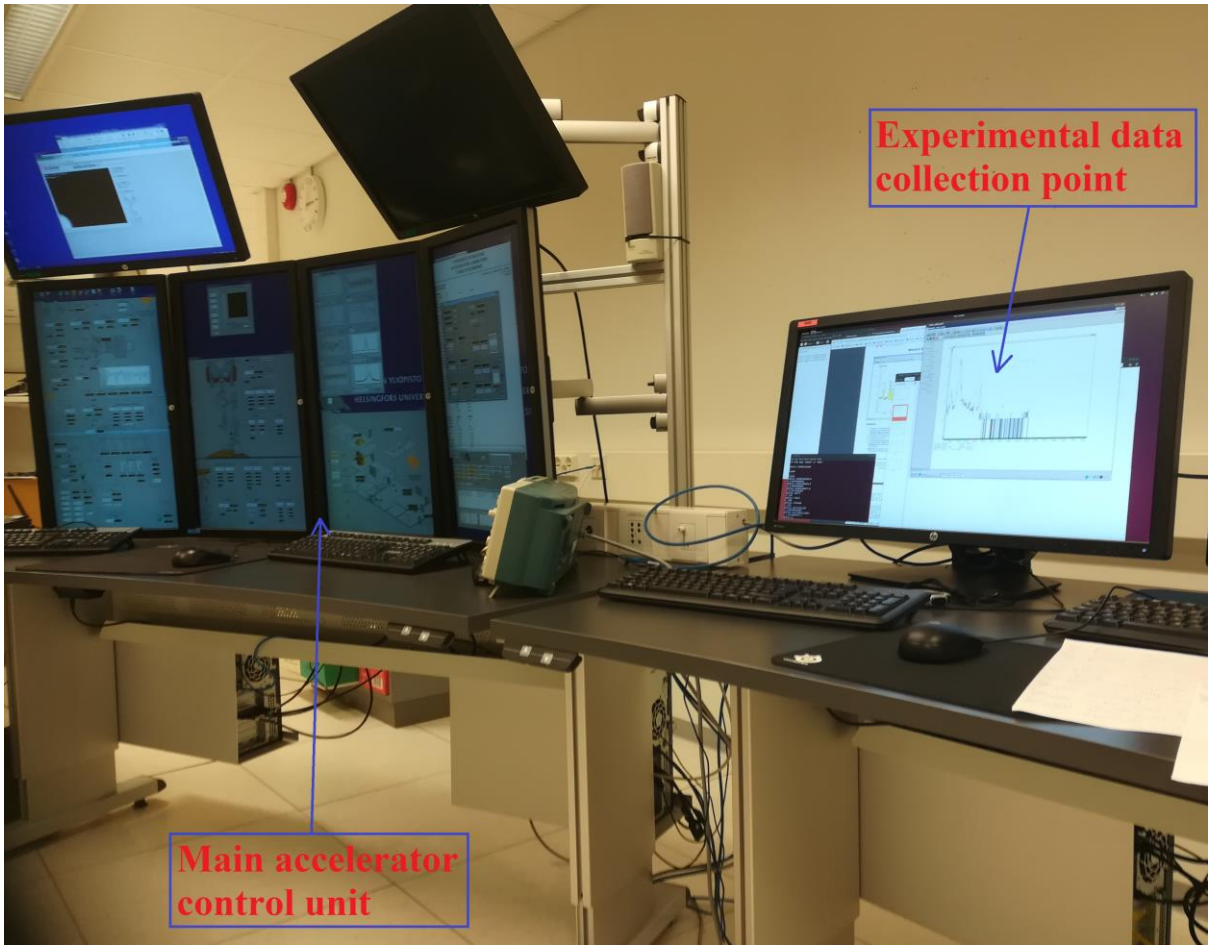

Figure 13: *Experimental data collection point with main accelerator control unit.*

3.3 Samples and experimental data

Samples and reference materials used in the external PIXE experiment are introduced. Moreover, sample preparation for the experiment has been discussed. In addition, the experimental data processing including an energy calibration and a background correction method with PyMCA software have been covered.

3.3.1 Introduction of samples and sample preparation

Nine coins from 18th to 20th centuries and from different countries have been used as the samples in the external PIXE experiment. These coins are presented in Figure 14 and Figure 15. Detailed information of the coins is presented in Table 1. The information has been collected from the International Catalog of World Coins [41].

Before the experiment, coins A - G have been removed from impurities in distilled water with ultrasonic sound cleaner. The cleaner utilizes an ultrasonic cleaning method, which consists of a simultaneous mechanical and chemical treatment of coins. A generator within the cleaner produces high-frequency sound vibrations, exerting a very strong mechanical action on a surface of each coin – this process can remove dirt, gunk, grime, and other impurities which have been built up on coins. At the same time, because of intense vibration of the metal surface of each coin, corrosion and other chemically formed foreign deposits are separated and removed. Coins H - I have not been cleaned with ultrasonic sound cleaner because these coins have been stored well in coin capsules. In addition, when cleaning coins ultrasonically, there is probability of overclean and cause damage to coins [42].

After the sample preparation each coin has been handled with rubber gloves to prevent any impurities on their surfaces. The coins A - I have been inserted to the sample holder one at a time and irradiated by the proton beam.

Figure 14: *Coins A - G used as target samples in the external PIXE experiment.*

Figure 15: *Coins H - I used as target samples in the external PIXE experiment.*

Coin	Country	Denomination	Year	Composition
A	USSR	15 kopeks	1922	silver 0.500
B	Russia	50 kopeks	1896	silver 0.900
C	USSR	1 ruble	1965	copper – zinc – nickel
D	Romania	100 lei	1944	nickel plated steel
E	USSR	1 ruble	1967	copper – zinc – nickel
F	USSR	1 ruble	1980	copper – nickel
G	USSR	1 ruble	1981	copper – nickel
H	France	5 francs	1961	silver 0.8333
I	Portugal	40 reis	1750	silver 0.917

Table 1: *Detailed information of coins A - I.*

3.3.2 Reference materials

Known compositions of four certified reference materials AGQ2, AGA1, AGA3, and AG500 have been irradiated in the same circumstances as the coins. This has been done to ease calibration of energies in the measurement data and to clarify identification of elements in the coins. Certificates of the reference materials utilized in the experiment are in **Appendix B: Reference materials**.

3.3.3 Experimental data analysis with PyMCA

Collected PIXE data from the experiment has been processed and analyzed in a PyMCA software that has been developed at the European Synchrotron Radiation Facility. The program

has been published as PyMCA because it has been written with a Python programming language and due to the scientific use of MCA for Multi-Channel Analyzer. PyMCA is a user-friendly program for analysis of energy-dispersive X-ray fluorescence data [43].

Energy calibration to each experimental data set has been performed with help of certified reference materials, which elements are well known. After the energy calibration all channel numbers of the coin data have been replaced with corresponding energies. In addition, an efficient background correction method of the PyMCA has been used to enhance the performance for the detection of peaks. The correction method consists of two steps: a background modelling and a background correction. After detecting some points which belong to the background from a spectrum, the background is modeled by a curve fitting method, separating detected x-ray peaks from the background with an analytical function. An example of processed data is presented in Figure 16. Each detectable spectral peak has been then identified based on its energy with the peak identifier tool of the PyMCA.

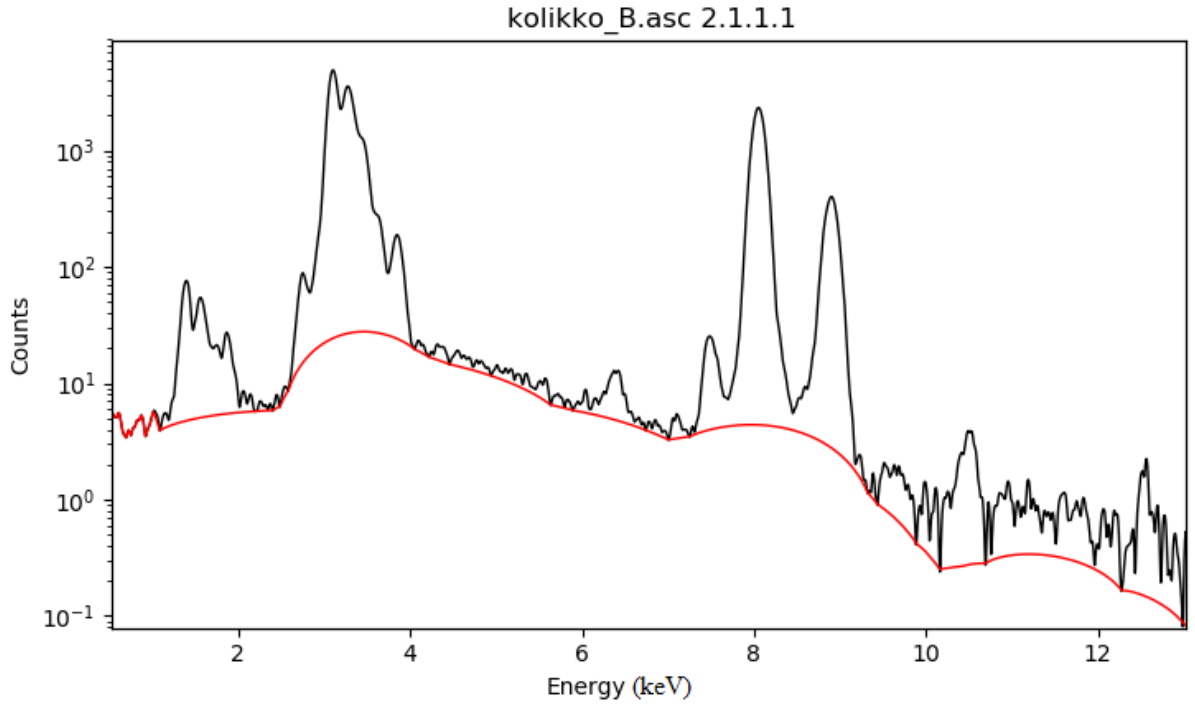

Figure 16: *PIXE spectrum of coin B after using the background correction method.*

4. RESULTS

X-ray peaks obtained from the processed data of each coin have been fitted and plotted based on possible x-ray emission lines and their characteristic x-ray energies. Moreover, each x-ray peak represents the presence of element for that specific energy. In general, K x-rays are detected easier for the lighter elements, whereas L x-rays for the heavier elements. Only clear and sharp peaks with low background noise have been considered.

In the first part, the results of processed data of silver coins are introduced – firstly the detection of x-rays is done with the SDD and secondly with the Ultra-LEGe detector. In the second part, the results of other coins (C, D, E, F, and G), which characteristic x-rays have been detected by the SDD, are discussed. Lastly, an overview of all obtained results is covered.

In measurements performed with the SDD, K x-ray peak of silicon (Si) has been observed. The presence of Si (K_α – 1.740 keV, K_β – 1.836 keV), is related to the Si_3N_4 of the exit window. Also, K x-ray peak of argon (Ar) has been detected. The presence of Ar (K_α – 2.957 keV, K_β – 3.190 keV) is related to the air. Si and Ar are present in every spectrum detected by the SDD, and therefore it will not be reported. In addition, at the beginning of every PIXE spectrum detected by the SDD, there is a high noise peak, as can be seen in appendices A.1 - A.12 of **Appendix A: Raw spectral data**. The noise peak of each raw data of is shown at very low energies, and it has been removed from the final PIXE spectra.

4.1 Silver coins

Silver coins A, B, H, and I have been irradiated in the external PIXE and detected first by the

SDD. After the measurements of all coins, the x-ray detector has been switched. Silver coins have been then irradiated again, and characteristic x-rays have been detected by the Ultra-LEGe detector.

4.1.1 Silver coins with SDD

Figure 17 shows a PIXE spectrum of x-rays in silver coin A detected by the SDD. In addition, the detected elements in the spectrum, their x-ray emission lines, and possible x-ray energies are presented in Table 2. PIXE spectra of other silver coins B, H, and I detected by the SDD including tables of determined elements, x-ray transmission lines, and energies are in **Appendix C: Results** (Appendices C.1 - C.6).

From the detected x-rays by the SDD, the following elements are identified in silver coins: silver (Ag), copper (Cu), arsenic (As), iron (Fe), copper (Cu), and zinc (Zn). Coins A and B have been observed to contain nickel (Ni). In addition, lead (Pb) has been detected in coins A, B, and I.

In case of detected L x-rays of As and Ag, broadened peaks can be seen in the PIXE spectrum of each silver coin. These peaks consist of cross sections of multiple L x-rays and includes ionization x-ray emissions of different energies. Possible L x-rays of Ag are presented in Table 2.

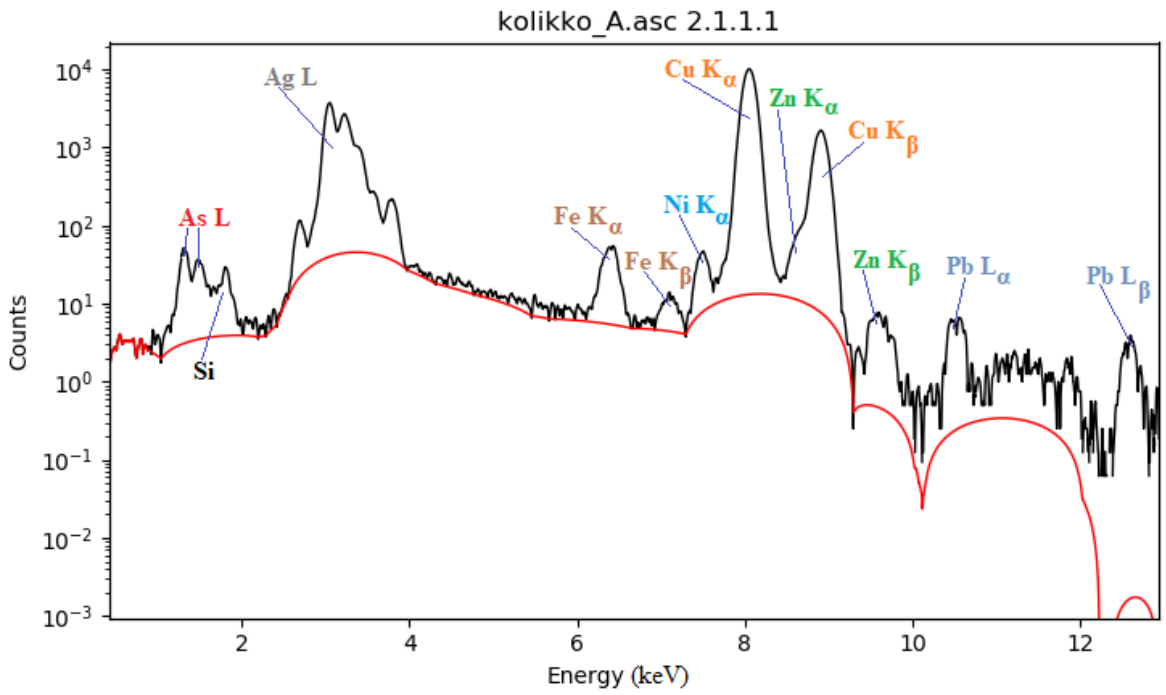

Figure 17: *PIXE spectrum of silver coin A detected by SDD.*

Element	X-ray emission line	Energy (keV)
As	L_3	1.282, 1.315
As	L_2	1.317, 1.350
As	L_1	1.380, 1.386, 1.485, 1.524
Ag	L_3	2.634, 2.978, 2.984, 3.256, 3.348
Ag	L_2	2.806, 3.151, 3.429, 3.520
Ag	L_1	3.203, 3.234, 3.433, 3.439, 3.743, 3.749
Fe	K_α	6.391, 6.404
Fe	K_β	7.058
Ni	K_α	7.461, 7.478
Cu	K_α	8.028, 8.048
Zn	K_α	8.616, 8.639
Cu	K_β	8.905
Zn	K_β	9.572
Pb	L_α	10.551
Pb	L_β	12.600, 12.614, 12.622

Table 2: *Detected elements, lines, and possible x-ray energies in coin A.*

From the experimental data of each silver coin, a presence of noise in the data can be observed with higher energy (above 10 keV). In case of silver coins, the only peaks detected above 10 keV are from Pb. The presence of Pb is totally random which can be explained for the metallurgic process of the obtaining of silver and for manufacturing process of the coins. Therefore, the data above 10 keV will not be discarded.

4.1.2 Silver coins with Ultra-LEGe detector

PIXE spectrum of silver coin A detected by the Ultra-LEGe detector is presented in Figure 18. In addition, detected spectral peaks with energies and elements of coin A are shown in Table 3. Experimental results of other silver coins, obtained in the same circumstances, are in **Appendix C: Results** (Appendices C.11 - C.16). The Ultra-LEGe detector detected following eight elements in silver coins: silver (Ag), copper (Cu), iron (Fe), lead (Pb), arsenic (As), tin (Sn), antimony (Sb), and bismuth (Bi).

The presence of germanium (Ge) in every PIXE spectrum detected by Ultra-LEGe detector can be clarified by a simple theoretical approach based on the production of germanium K x-rays (K_α – 9.855 keV, K_β – 11.101 keV) inside the Ge crystal of the detector. In addition, there is one peak at 13.9 keV which is also present in every x-ray spectrum by Ultra-LEGe detector. This peak does not correspond any reasonable element, and for that reason will not be considered. In addition, in the PIXE spectra of coins A and B, there is a sum peak (at 17.3-19.8 keV) which has been recorded due to Ge.

From the PIXE spectra obtained by the Ultra-LEGe detector most of the elements are detected with a great accuracy between 6 - 26 keV. Before Above 30 keV it is hard to detect any clear peak due to presence of noise effect. In addition, there are sum peaks astride 45 keV. Sum peaks can be observed in Appendices A.13 - A.20 of **Appendix A: Raw spectral data**

astride the channel 2500**.**

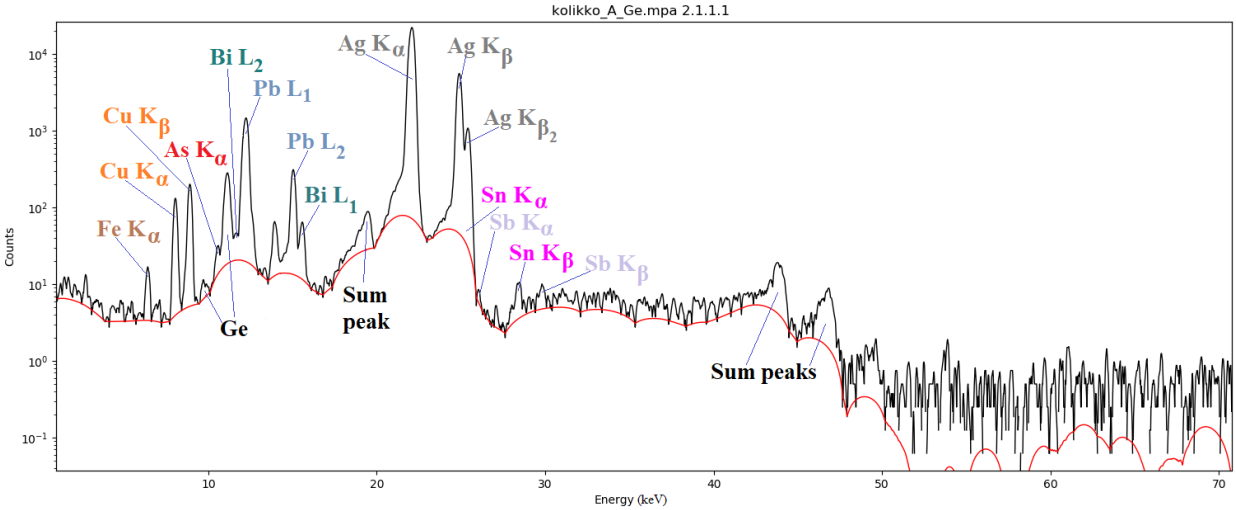

Figure 18: *PIXE spectrum of silver coin A detected by Ultra-LEGe detector.*

Element	X-ray emission line	Energy (keV)
Fe	K_α	6.391, 6.404
Cu	K_α	8.028, 8.048
Cu	K_β	8.905
As	K_α	10.544
Bi	L_2	11.712
Pb	L_1	12.307
Pb	L_2	15.503
Bi	L_1	15.582
Ag	K_α	21.990
Ag	K_β	24.912, 24.943
Sn	K_α	25.271
Ag	$K_{\beta 2}$	25.451, 25.458
Sb	K_α	26.111, 26.359
Sn	K_β	28.444, 28.486
Sb	K_β	29.726

Table 3: *Detected elements, lines, and possible x-ray energies in coin A.*

4.2 Other coins

All other coins, which did not contain any silver, have been detected by the SDD only. The results of other coins are presented in Figures 19 - 21 and Tables 4 - 6, as well as in **Appendix C: Results** (Appendices C.7 - C.10).

These coins have been classified into three groups based on their metallic composition (presented in Table 1): nickel plated steel (coin D), copper-zinc-nickel (coins C and E), and copper-nickel (coins F and G).

From the PIXE spectra of the coins of each group, a presence of noise in x-ray energy above 10 keV can be observed. In addition, there are significantly high x-ray peaks between 14.883 - 16.738 keV. These x-ray peaks are clearly sum peaks of the highest peaks in each PIXE spectrum.

4.2.1 Nickel plated steel

Results of nickel plated steel coin D are presented in Figure 19 and in Table 4. The results show that besides iron (Fe) and nickel (Ni) coin D also contains cobalt (Co) and copper (Cu).

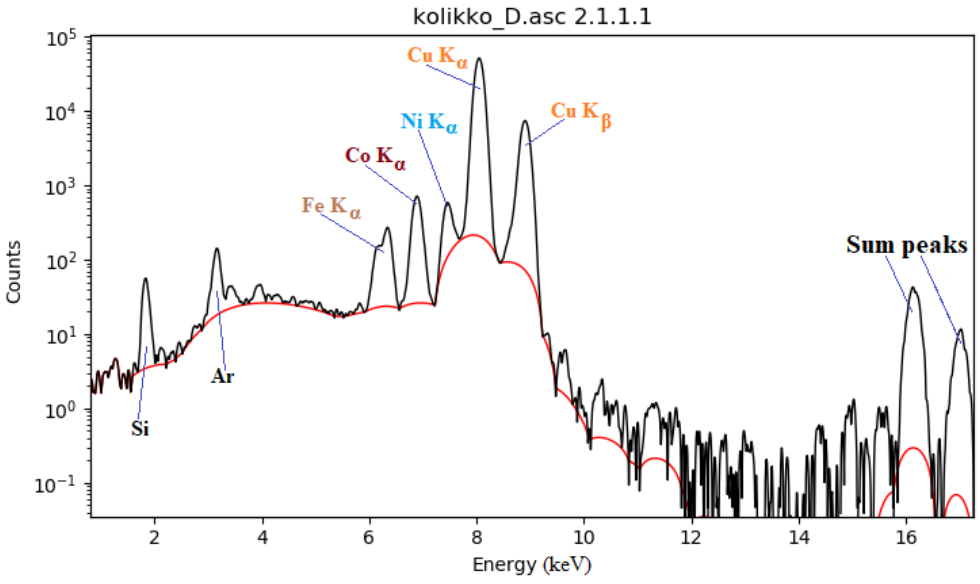

Figure 19: *PIXE spectrum of coin D detected by SDD.*

Element	X-ray emission line	Energy (keV)
Fe	K_α	6.391, 6.404
Co	K_α	6.915, 6.930
Ni	K_α	7.461, 7.478
Cu	K_α	8.028, 8.048
Cu	K_β	8.905

Table 4: *Detected elements, lines, and possible x-ray energies in coin D.*

4.2.2 Copper – zinc – nickel

Coins C and E have an alloy of copper-zinc-nickel. In both coins, same five elements have been detected, namely, manganese (Mn), iron (Fe), nickel (Ni), copper (Cu), and zinc (Zn). The PIXE spectrum of coin C is presented in Figure 20. In addition, detected elements, lines, and x-ray energies of coin C are tabulated in Table 5. Experimental results of coin E are presented in Appendices C.7 and C.8.

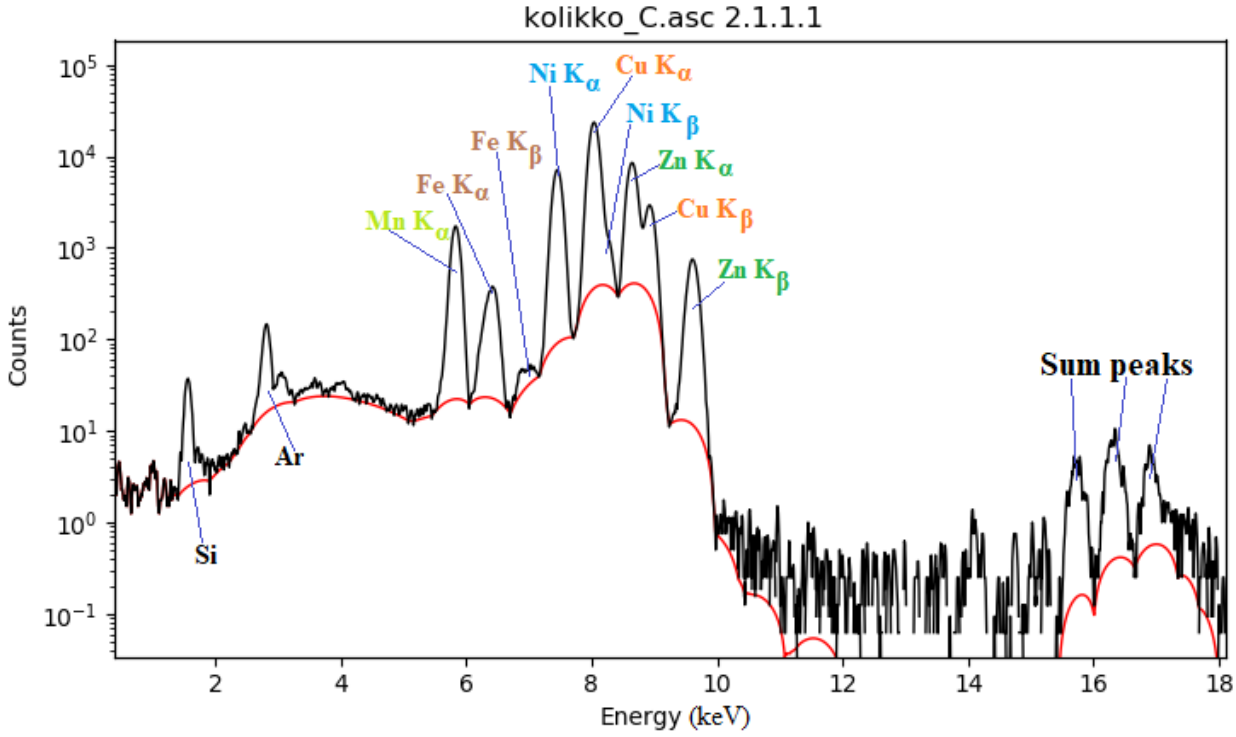

Figure 20: *PIXE spectrum of coin C detected by SDD.*

Element	X-ray emission line	Energy (keV)
Mn	K_α	5.888, 5.899
Fe	K_α	6.391, 6.404
Fe	K_β	7.058
Ni	K_α	7.461, 7.478
Cu	K_α	8.028, 8.048
Ni	K_β	8.265
Zn	K_α	8.616, 8.639
Cu	K_β	8.905
Zn	K_β	9.572

Table 5: *Detected elements, lines, and possible x-ray energies in coin C.*

4.2.3 Copper – nickel

Coins F and G have been both approved throughout the PIXE experiment to have an alloy of copper-nickel. The results obtained from the PIXE measurement of coin F are presented in Figure 21 and in Table 6. The results of coin G are in **Appendix C: Results** (Appendices C.9 and C.10). Both coins consist of copper (Cu), nickel (Ni), iron (Fe), and manganese (Mn).

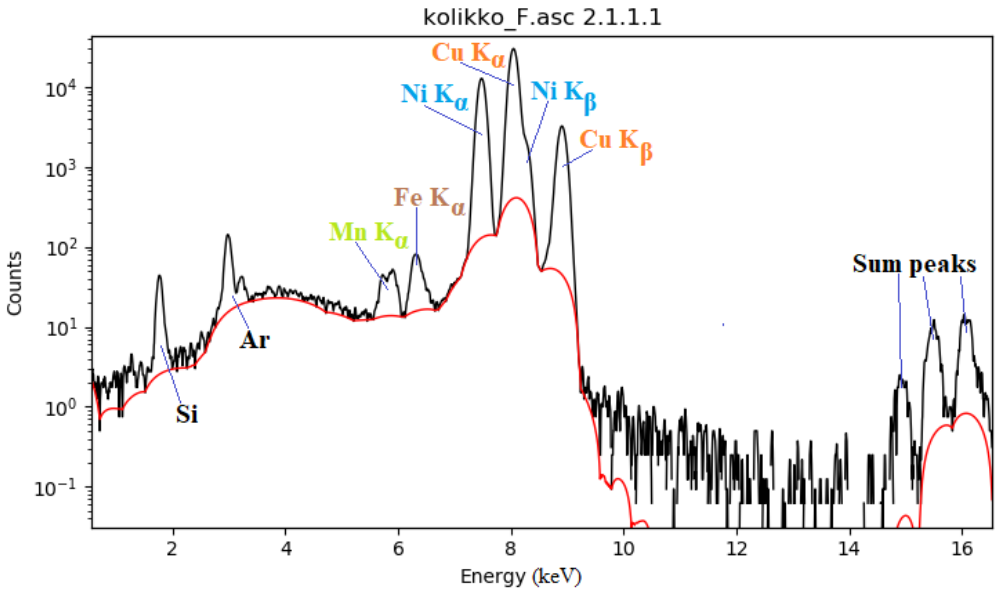

Figure 21: *PIXE spectrum of coin F detected by SDD.*

Element	X-ray emission line	Energy (keV)
Mn	K_α	5.888, 5.899
Fe	K_α	6.391, 6.404
Ni	K_α	7.461, 7.478
Cu	K_α	8.028, 8.048
Ni	K_β	8.265
Cu	K_β	8.905

Table 6: *Detected elements, lines, and possible x-ray energies in coin F.*

4.3 Overview of results

The major components of studied silver coins (coins A, B, H, and I) are Ag and Cu. Both metals are found pure in nature, and they both have face-centered cubic (FCC) crystal structure. Pure elements have identical atoms arranged in regular layers which slide easily over each other. This is the reason why these metals are soft and need to be made harder to afford coins greater durability. Harder structure can be achieved by adding other elements to pure metals, which is known as forming an alloy. This can be explained by that the alloy has different sized atoms of the mixed metals, which makes its atomic layers less regular. From the PIXE spectra of the SDD, seven elements have been determined. In the measurements with Ultra-LEGe detector, eight elements have been discovered, of which five elements are the same as in the SDD measurements. All elements obtained from the PIXE measurements of silver coins are consistent with other similar studies [44, 45].

In nickel plated steel coin (coin D) observed elements are Fe, Cu, Co, and Ni. Steel is an

alloy consisting of Fe with typically a few percent of carbon (C). Neither of the x-ray detectors employed in the study cannot detect very low energy x-rays (less than 0.5 keV). Cu is often added to steel to increase its corrosion resistance and prevent formation of rust. Co is normally used as an alloying addition. Ni plating produces a coating to steel and adds more corrosion resistance and hardness.

Copper-nickel-zinc alloy coins (coins C and E) have been observed to consist of Cu, Ni, and Zn with additions of Mn and Fe. At the beginning, commemorative rubles have been struck in the same alloy as other circulating coins. Starting from year 1975, copper-nickel-zinc alloy has been changed to a higher-quality copper-nickel alloy which excluded Zn in the composition of coins [46]. This explains why USSR coins C (1965) and E (1967) contain Zn, whereas coins G (1980) and F (1981) do not. Experimental results of the present study verify this.

Copper-nickel, which is also known as cupronickel, is an alloy of Cu that contains Ni and strengthening elements, such as Fe and Mn. All these four elements have been found in the measurements of coins F and G.

5. CONCLUSIONS

In the present study, nine coins have been analyzed in the laboratory by the PIXE technique to qualitatively determine their elemental composition. The external PIXE measurement setup provides nondestructive, sensitive, and fast multi-elemental analysis method with an excellent identification accuracy of elemental signals.

The theory part of this thesis explains the most fundamental parts of interactions between the external ion beam and the target sample. PIXE is based on detecting characteristic x-rays which are formed during the transitions of electrons. These processes occur when an inner shell electron is released from an atom.

Each coin has been exposed to the 3 MeV external proton beam in the experimental box. Emitted characteristic x-rays have been detected prompt during beam exposure by the x-ray detector and recorded as a spectral peak with the aid of MCA and the other electronic devices of the experimental setup. A quantitative analysis of the obtained raw spectral data of each measurement has been performed with the PyMCA software. K x-rays and L x-rays of many elements have been identified. Obtained experimental results verify that the external PIXE technique can be utilized as a practical tool for the identification of elements in metallurgical samples.

Before the ion beam exposure on the sample, most of the coins have been removed from impurities in distilled water with ultrasonic sound cleaner. This ultrasonic cleaning method provided a simultaneous mechanical and chemical treatment of coins. This procedure has a great impact in obtaining more accurate results.

From the point of view of the numismatics, the application of PIXE method provides valuable information of coins, for example in changes of material technologies, economic conditions, political aspects, monetary theory, and art of coin design.

Due to simplicity of PIXE analysis method, it can be utilized in numerous applications

and in wide range of fields, such as materials science, archaeology, medicine, criminal investigations, and as contamination monitoring of food.

REFERENCES

[1] A. Ene, I. V. Popescu, C. Stihi, "Applications of proton-induced X-ray emission technique in materials and environmental science", *Ovidius University Annals of Chemistry*, 20, No. 1 (2009): 35-39.

[2] A. E. Pillay, "Analysis of Archaeological Artefacts: PIXE, XRF or ICP-MS?", *Journal of Radioanalytical and Nuclear Chemistry*, 247, No. 3 (2001): 593-595.

[3] W. Maenhaut, "Particle-induced x-ray emission spectrometry: An accurate technique in the analysis of biological, environmental and geological samples", *Analytica Chimica Acta*, (1987): Vol. 195: 125-140.

[4] B. B. Tripathy, T. R. Rautray, A. C. Rautray, V. Vijayan, "Elemental analysis of silver coins by PIXE technique", *Applied Radiation and Isotopes*, (2010): Vol. 68: 454-458.

[5] A. Scherl, "Das Grosse Buch der Technik", *Verlag für Wissen und Bildung / Bertelsmann*, (1961): 191.

[6] S. A. E. Johansson, J. L. Campbell, "PIXE: A novel technique for elemental analysis", *Wiley*, (1988): Vol. 47.

[7] T. B. Johansson, R. Akselsson, S. A. E. Johansson, "X-ray analysis: Elemental trace analysis at the 10^{-12} g level", *Nuclear Instruments and Methods*, (1970): Vol. 84: 141-143.

[8] S. A. E. Johansson , J. L. Campbell, K. G. Malmqvist, J. D. Winefordner, “Particle-Induced X-Ray Emission Spectrometry (PIXE)”, *Wiley*, (1995): Ch. 1: 1-16.

[9] S. Gasiorowicz, “Quantum Physics”, *Wiley*, 3rd Ed., (2003): Ch. 14.3 & 17.3.

[10] S. A. E. Johansson , J. L. Campbell, K. G. Malmqvist, J. D. Winefordner, “Particle-Induced X-Ray Emission Spectrometry (PIXE)”, *Wiley*, (1995): Ch. 1: 1-16.

[11] W. Bambynek, B. Crasemann, R. W. Fink, H. U. Freund, H. Mark, C. D. Swift, R. E. Price, P. Venugopala Rao, “X-Ray Fluorescence Yields, Auger, and Coster-Kronig Transition Probabilities”, *Reviews of Modern Physics*, (1972): Vol. 44: 716.

[12] K. Ishii, “PIXE and Its Applications to Elemental Analysis”, *Quantum Beam Science*, (2019).

[13] B. Deghfel, A. Kahoul, A. Abdellatif, M. Nekkab, “Proton induced K-shell ionization cross sections for a wide range of elements ($4 \leq Z \leq 92$) within ECPSSR theory and updated experimental data”, *Journal of Radiation Research and Applied Sciences*, (2014): Vol. 7: 607-613.

[14] S. Ouziane, A. Amokrane, M. Zilabdi, “Experimental measurements of X-ray production cross-sections by protons of energies between 1 and 2.3 MeV and comparison with theoretical predictions of PWBA and ECPSSR models”, *Nuclear Instruments and Methods in Physics Research Section B: Beam Interactions with Materials and Atoms*, (2000): Vol. 161-163: 141-144.

[15] W. Brand, G. Lapicki, “Energy-loss effect in inner-shell Coulomb ionization by heavy charged particles”, *Physical Review A*, (1981): Vol. 23: 1717.

[16] W. Brand, G. Lapicki, “Coulomb deflection in ion-atom collisions”, *Physical Review A*, (1979): Vol. 20: 481.

[17] G. Lapicki, “The status of theoretical K-shell ionization cross sections by protons”, *X-Ray Spectrometry*, (2005): Vol. 34: 269-278.

[18] F. S. Olise, F. I. Nana, A. D. Aladese, “Proton induced L-shell cross-sections for some post-transition metals: A comparison of ECPSSR and SCA models”, *Nuclear Instruments and Methods in Physics Research Section B: Beam Interactions with Materials and Atoms*, (2020): Vol. 472: 1-6.

[19] G. Lapicki, “Cross Sections for K-shell X-ray Production by Hydrogen and Helium Ions in Elements from Beryllium to Uranium”, *Journal of Physical and Chemical Reference Data*, (1989): Vol. 18: 111.

[20] K. Ishii, S. Morita, “CONTINUOUS BACKGROUNDS IN PIXE”, *International Journal of PIXE*, (1990): Vol. 1: 1-29.

[21] K. Ishii, H. Yamazaki, S. Matsuyama, W. Galster, T. Satoh, M. Budnar, “Contribution of atomic bremsstrahlung in PIXE spectra and screening effect in atomic bremsstrahlung”, *X-Ray Spectrometry*, (2005): Vol. 34: 363-365.

[22] K. Ishii, S. Morita, “Continuum x rays produced by light-ion—atom collisions”, *Physical Review A*, (1984): Vol. 30: 2278-2286.

[23] K. Ishii, “Contribution of atomic bremsstrahlung in PIXE spectra and screening effect in atomic bremsstrahlung”, *X-Ray Spectrometry*, (2005): Vol. 34: 363-365.

[24] A. Yamadera, K. Ishii, K. Sera, M. Sebata, S. Morita, “Quasifree-electron bremsstrahlung induced by the projectile”, *Physical Review A*, (1981): Vol. 23 & 24.

[25] K. Murozono, K. Ishii, H. Yamazaki, S. Matsuyama, S. Iwasaki “Pixe spectrum analysis taking into account bremsstrahlung spectra”, *Nuclear Instruments and Methods in Physics Research Section B: Beam Interactions with Materials and Atoms*, (1999): Vol. 150: 76-82.

[26] K. Ishii, “High energy limit of atomic bremsstrahlung”, *Nuclear Instruments and Methods in Physics Research Section B: Beam Interactions with Materials and Atoms*, (1995): Vol. 99: 163-165.

[27] J. Zeb, S. Ali, M. Haneef, A. M. Naeem, J. Akbar, “Standardization of proton induced X-ray emission for analysis of trace elements in thick samples”, *Canadian Journal of Physics*, (2018).

[28] S. A. E. Johansson, “PIXE: a novel technique for elemental analysis”, *Endeavour*, (1989): Vol. 13: 48-53.

[29] The facilities with ion beams of the Helsinki Accelerator Laboratory:

https://www.helsinki.fi/en/researchgroups/helsinki-accelerator-laboratory/facilities/accelerators

[30] Source of Negative Ions by Cesium Sputtering (SNICS):

https://www.pelletron.com/products/snics/

[31] Van De Graaff Generator:

https://www.imagesco.com/articles/high-voltage/van_de_graaf.html

[32] G. Choppin, J. Liljenzin, J. Rydberg, "Radiochemistry and Nuclear Chemistry", *Butterworth-Heinemann*, 3rd Ed., (2001): Ch. 13.4.: 352-353.

[33] Constant-Voltage Accelerators:

https://www.britannica.com/technology/particle-accelerator/Constant-voltage-accelerators#ref365027

[34] V. Palonen, K. Mizohata, T. Nissinen, J. Räisänen, "External beam IBA set-up with large-area thin Si_3N_4 window", *Nuclear Instruments and Methods in Physics Research B*, (2016): Vol. 380: 11-14.

[35] P. A. Mandò, "Advantages and limitations of external beams in applications to arts & archeology, geology and environmental problems", *Nuclear Instruments and Methods in Physics Research B*, (1994): Vol. 85: 815-823.

[36] Key parameters of KETEK Silicon Drift detector (AXAS-D) with VITUS H20 module:

https://www.ketek.net/sdd/vitus-sdd-modules/vitus-h20/

[37] Silicon Drift Detectors Explained:

https://www.exvil.lt/wp-content/uploads/2012/04/SDD_Explained.pdf

[38] Canberra Ultra-LEGe Detector:

http://hea-www.cfa.harvard.edu/~bradw/HXDS/projects/axaf/2ultlege.pdf

[39] Germanium Detectors User's Manual:

https://www.researchgate.net/profile/Jan_Hansman/post/What_does_the_mean_of_freezing_the_endcap_of_HPGe_which_is_cooled_by_X-cooler/attachment/59d63f4e79197b807799bc04/AS%3A426817950621703%401478772737927/download/Germanium_Detectors_Manual.pdf

[40] Ultra-Low Energy Germanium Detectors:

https://mirion.s3.amazonaws.com/cms4_mirion/files/pdf/spec-sheets/c40696_ultra-lege_det_super_spec_3.pdf?1557863599

[41] International Catalog of World Coins: https://en.ucoin.net/

Coin A: https://en.ucoin.net/coin/ussr-15-kopeks-1922/?cid=8925

Coin B: https://en.ucoin.net/coin/russia-50-kopeks-1896/?cid=24526&vid=9606

Coin C: https://en.ucoin.net/coin/ussr-1-ruble-1965/?cid=4159

Coin D: https://en.ucoin.net/coin/romania-100-lei-1944/?cid=38308

Coin E: https://en.ucoin.net/coin/ussr-1-ruble-1967/?tid=4191

Coin F: https://en.ucoin.net/coin/ussr-1-ruble-1980/?tid=4199

Coin G: https://en.ucoin.net/coin/ussr-1-ruble-1981/?tid=4201

Coin H: https://en.ucoin.net/coin/france-5-francs-1961/?cid=7267

Coin I: https://en.ucoin.net/coin/portugal-40-reis-1750/?tid=87163

[42] A Complete Guide To Cleaning, Preservation and Conservation of Coins, page 14: https://www.metaldetectingworld.com/cleaning_coin_p14_ultrasonics.shtml

[43] V.A. Solé, E. Papillon, M. Cotte, Ph. Walter, J. Susini, "A multiplatform code for the analysis of energy-dispersive X-ray fluorescence spectra", *Spectrochimica Acta Part B*, (2007): Vol. 62: 63-68.

[44] M. Hajivaliei, M. L. Garg, D. K. Handa, K. L. Govil, T. Kakavand, V. Vijayan, K. P. Singh, I. M. Govil, "PIXE analysis of ancient Indian coins", *Nuclear Instruments and Methods in Physics Research Section B: Beam Interactions with Materials and Atoms*, (1999): Vol. 150: 645-650.

[45] C. Flamenta, P. Marchetti, "Analysis of ancient silver coins", *Nuclear Instruments and Methods in Physics Research Section B: Beam Interactions with Materials and Atoms*, (2004): Vol. 226: 179-184.

[46] Монеты СССР и России: https://ru-moneta.ru/catalog/1rub-1961-1991/1-rubl-1975-goda-tsena/

APPENDICES

Appendix A: Raw spectral data

Appendix B: Reference materials

Appendix C: Results

Appendix A: Raw spectral data

Raw spectral data detected by the SDD is presented in Appendices A.1 - A.12. In addition, Appendices A.13 - A.20 represent raw spectral data detected by the Ultra-LEGe detector.

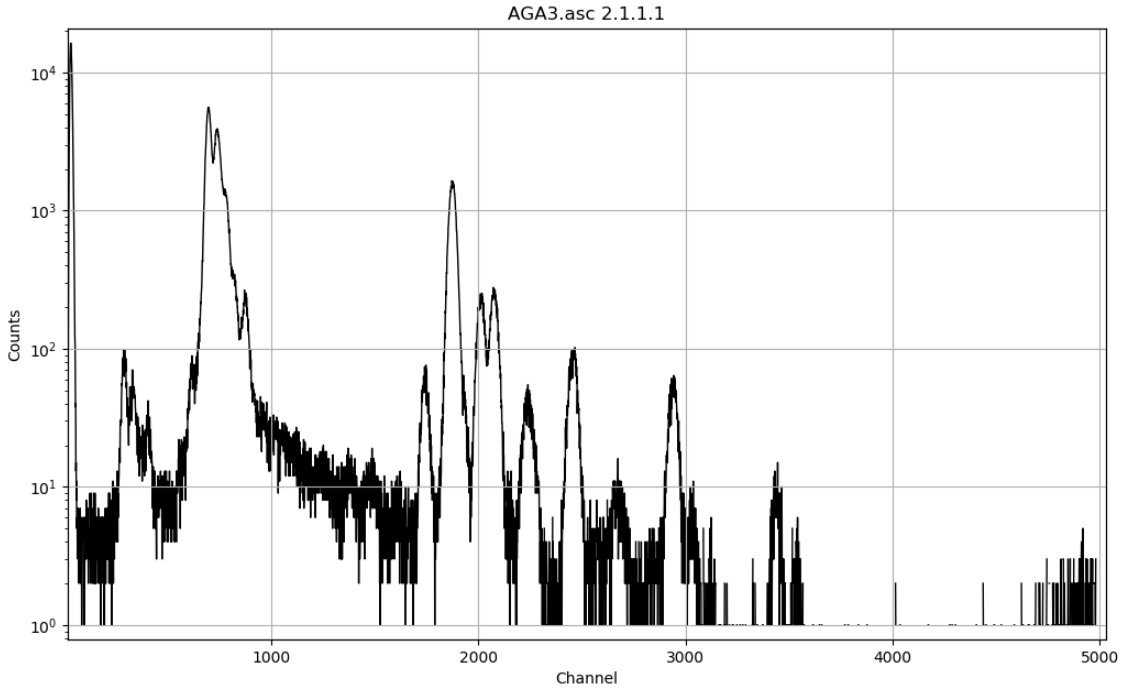

Appendix A.1: *Raw spectral data of reference material AGA3 detected by SDD.*

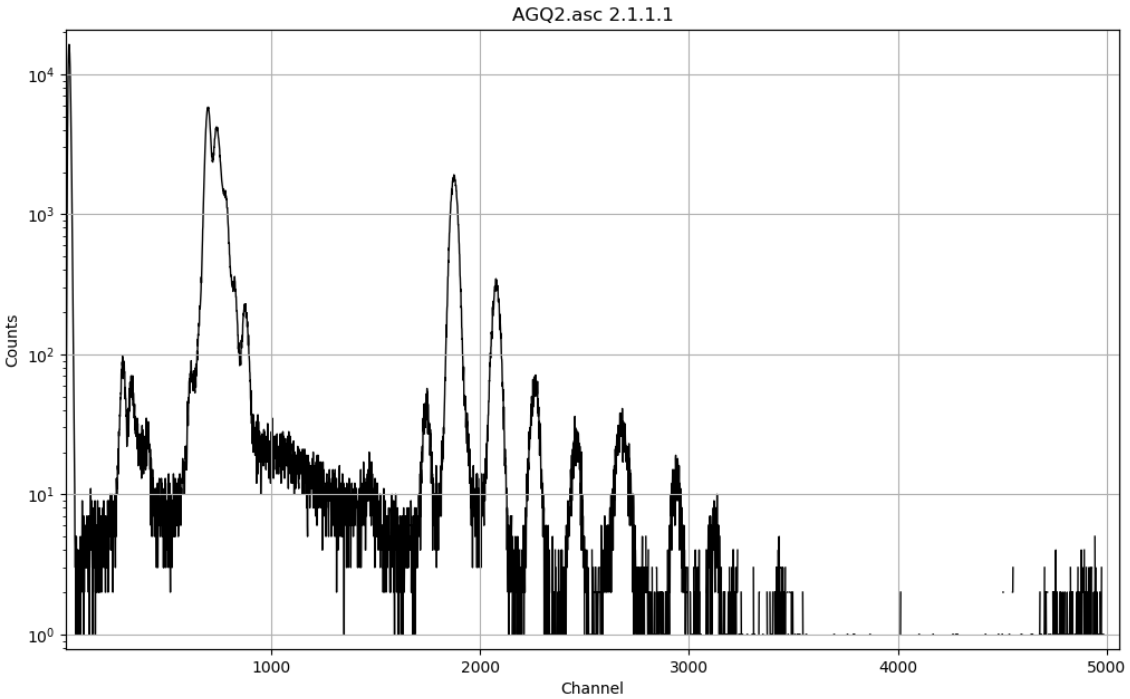

Appendix A.2: *Raw spectral data of reference material AGQ2 detected by SDD.*

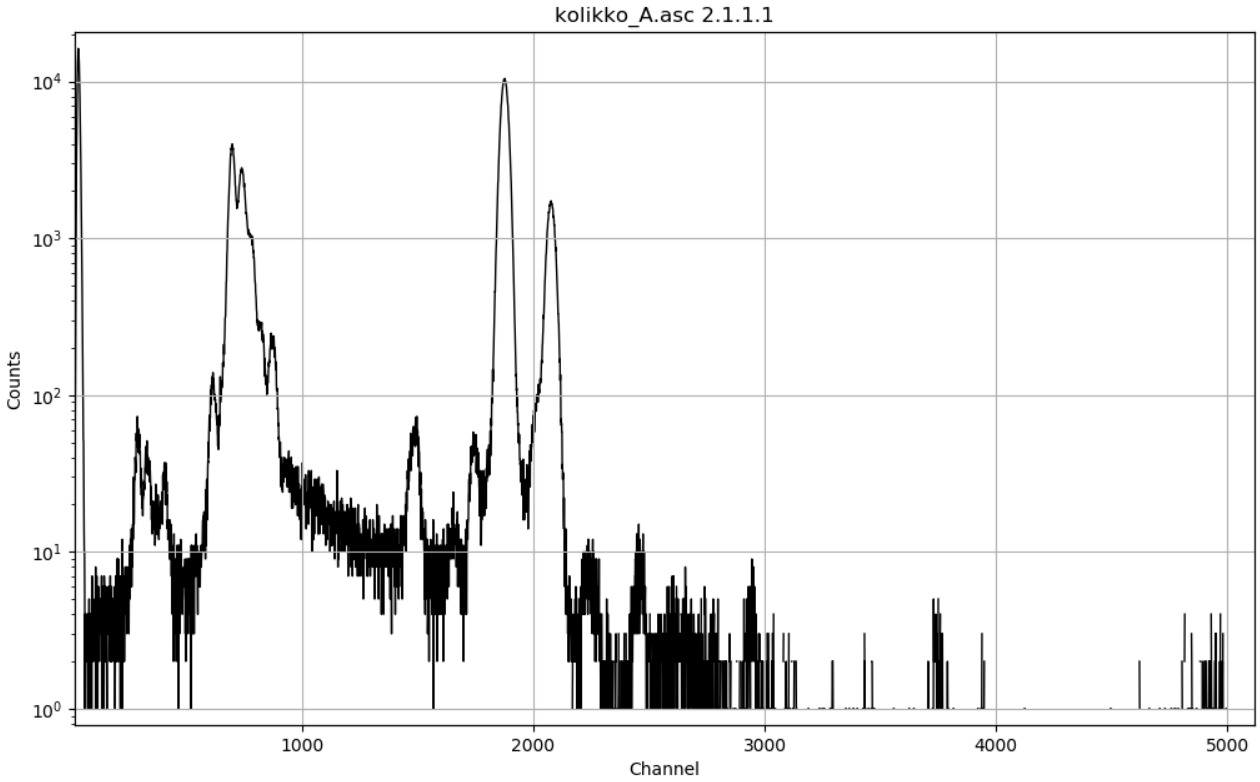

Appendix A.3: *Raw spectral data of coin A detected by SDD.*

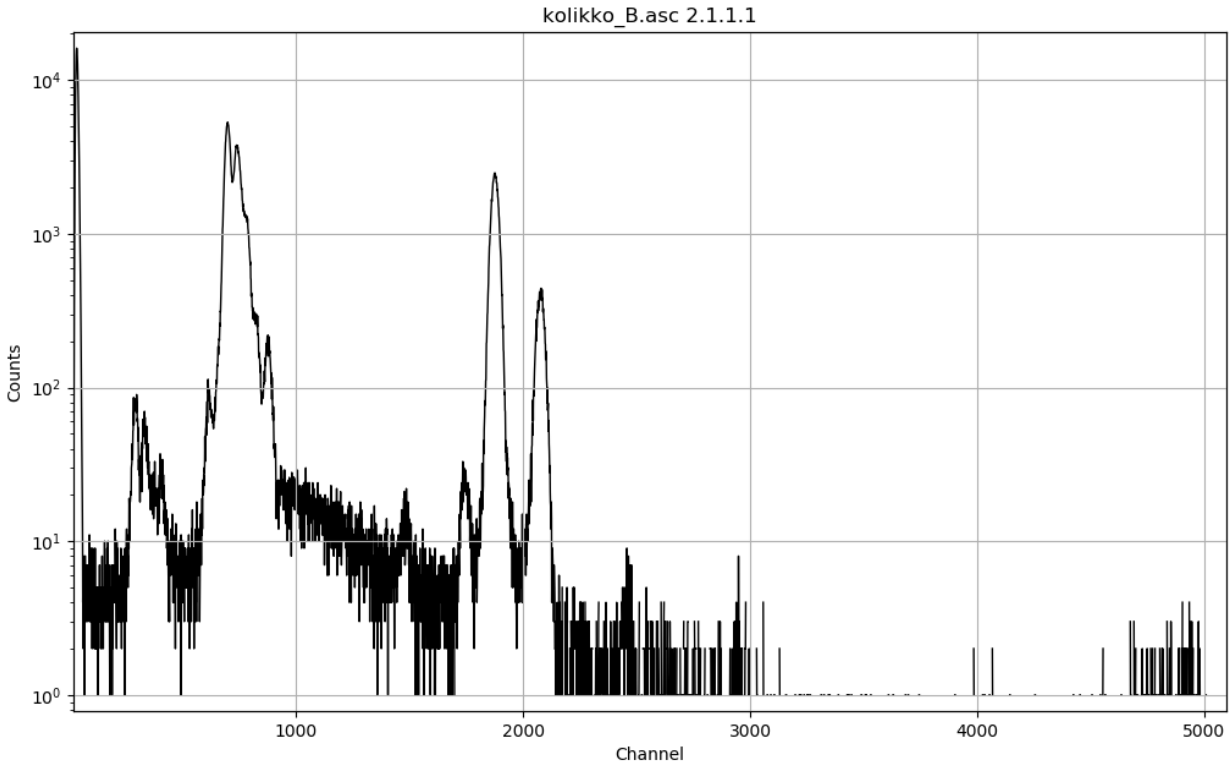

Appendix A.4: *Raw spectral data of coin B detected by SDD.*

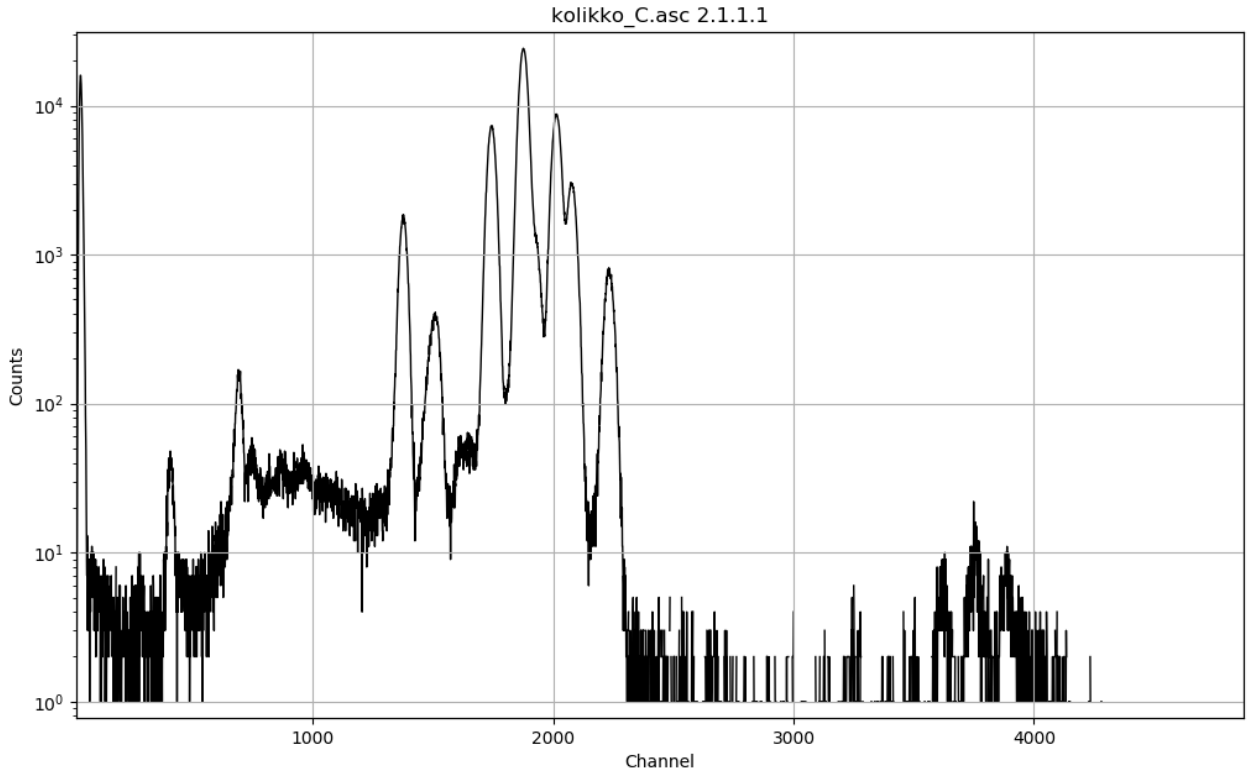

Appendix A.5: *Raw spectral data of coin C detected by SDD.*

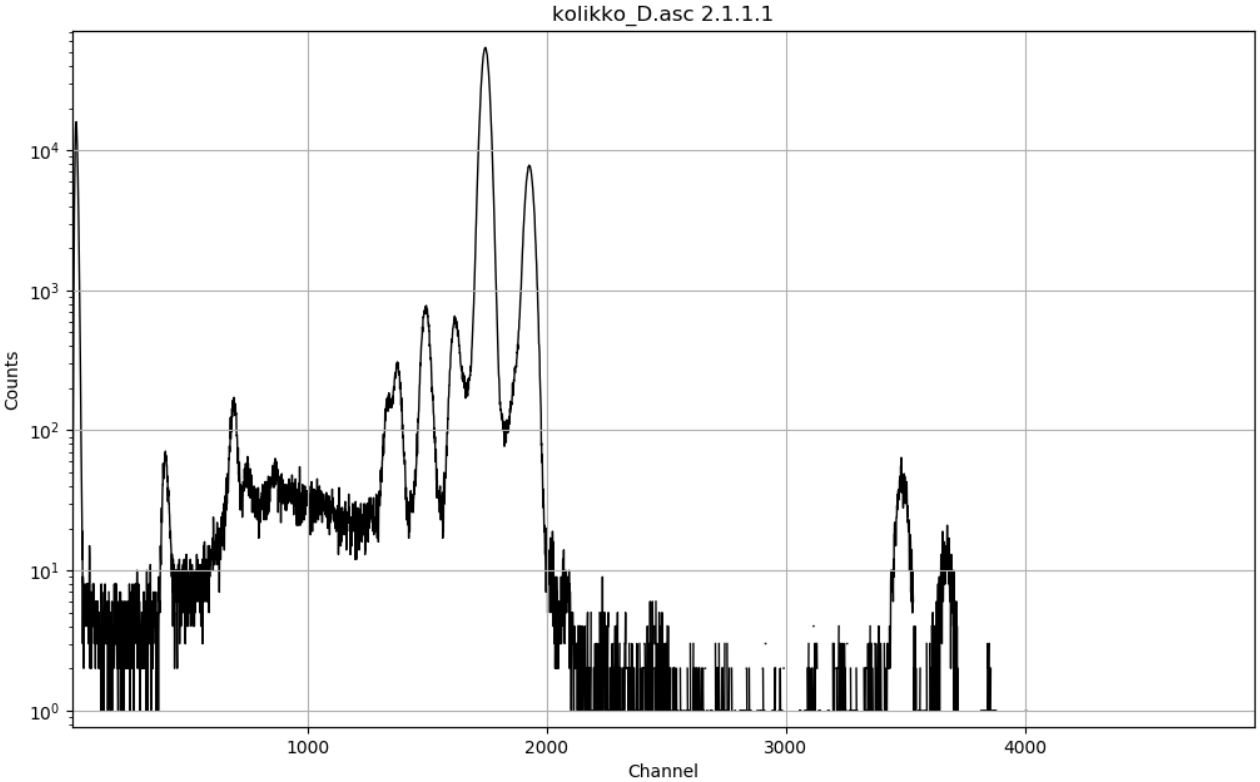

Appendix A.6: *Raw spectral data of coin D detected by SDD.*

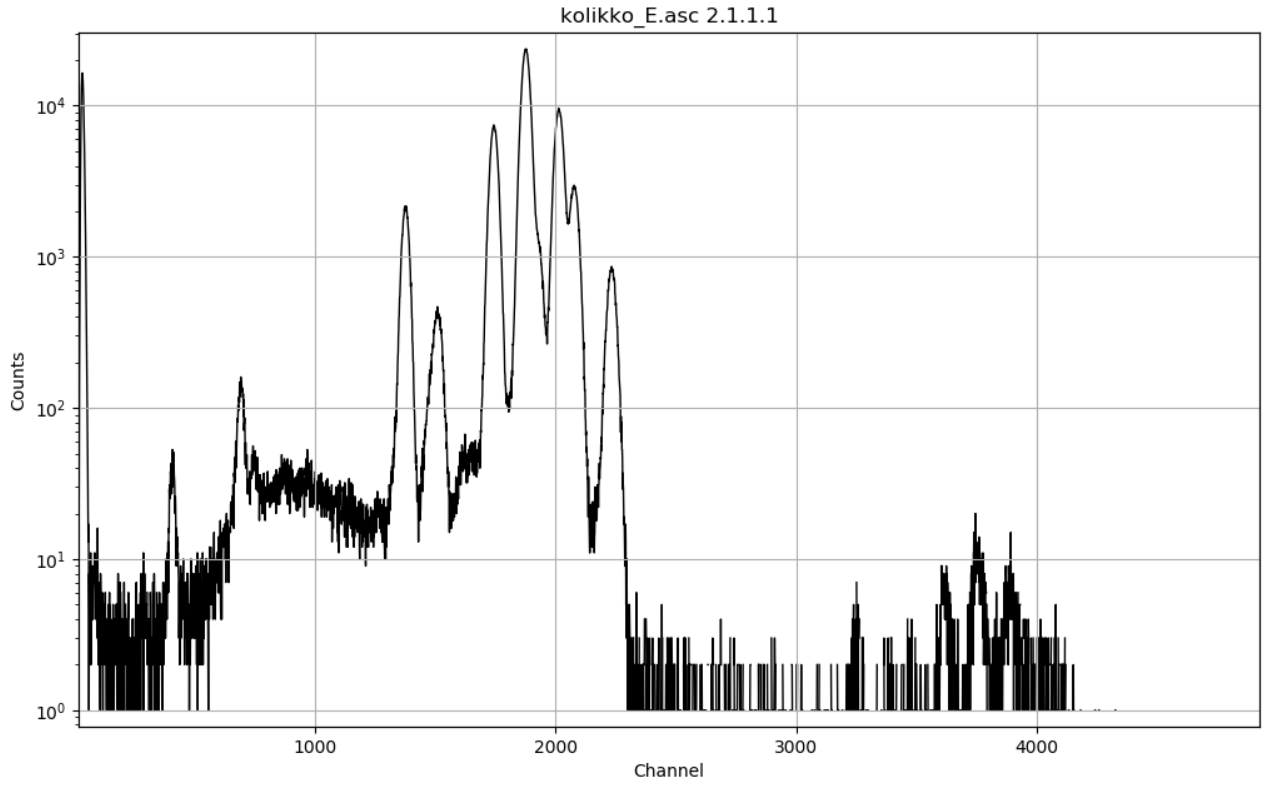

Appendix A.7: *Raw spectral data of coin E detected by SDD.*

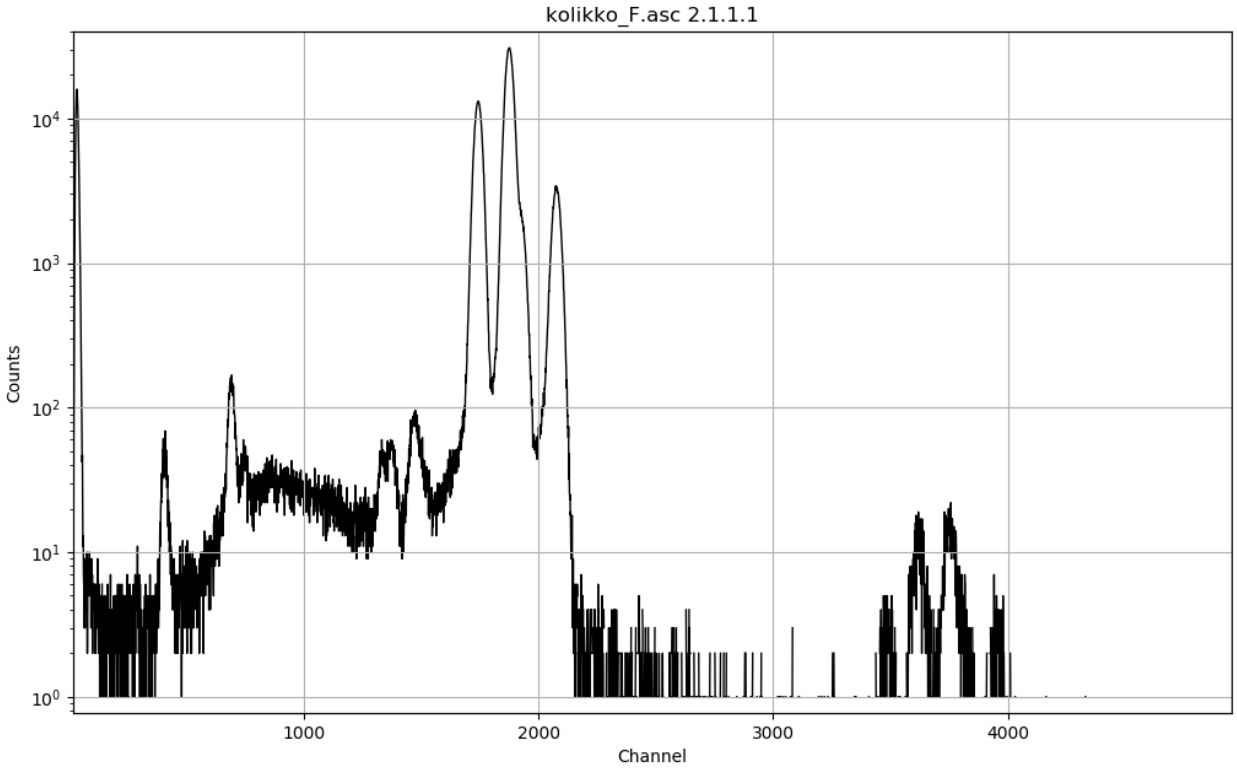

Appendix A.8: *Raw spectral data of coin F detected by SDD.*

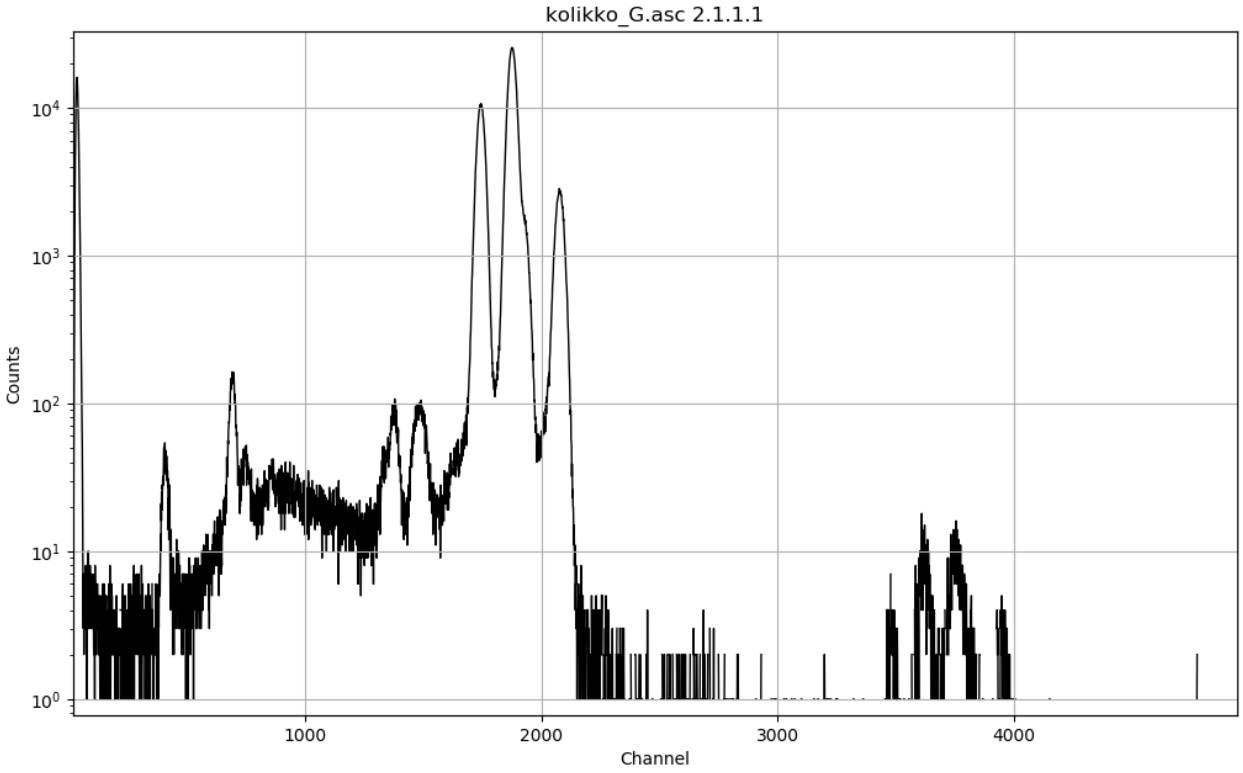

Appendix A.9: *Raw spectral data of coin G detected by SDD.*

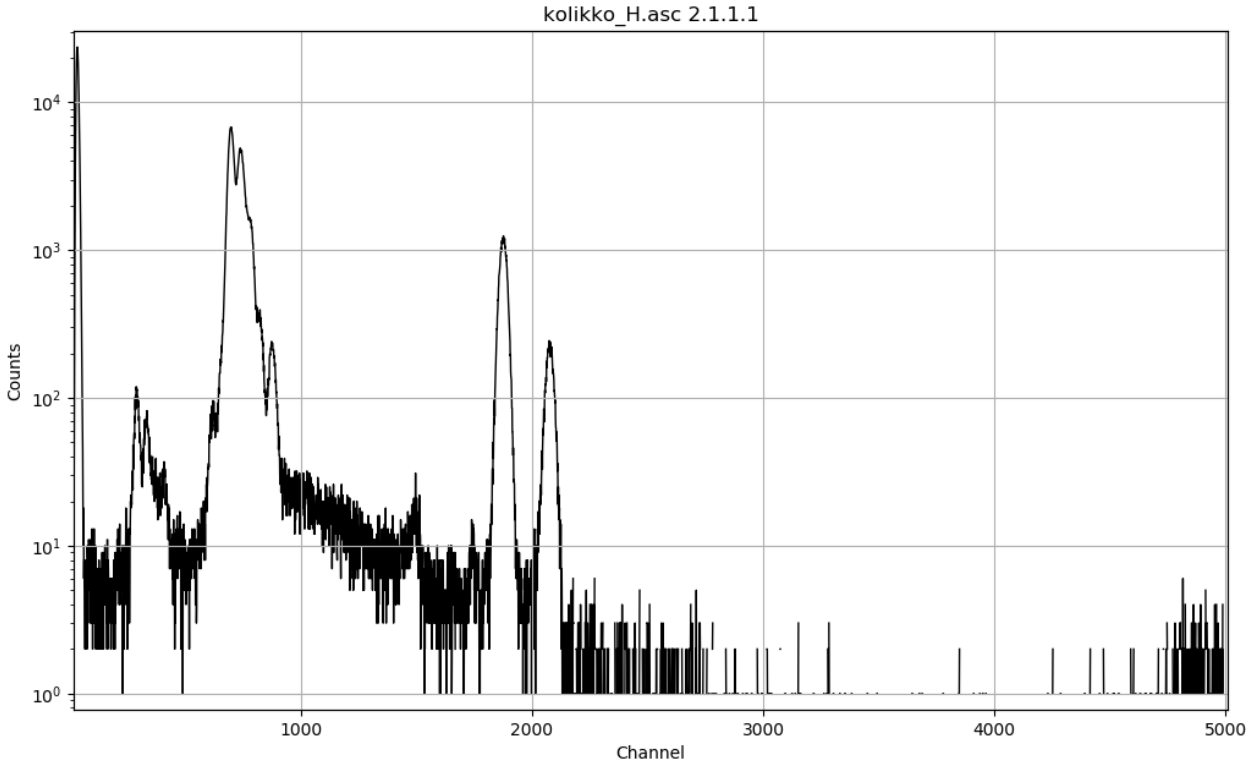

Appendix A.10: *Raw spectral data of coin H detected by SDD.*

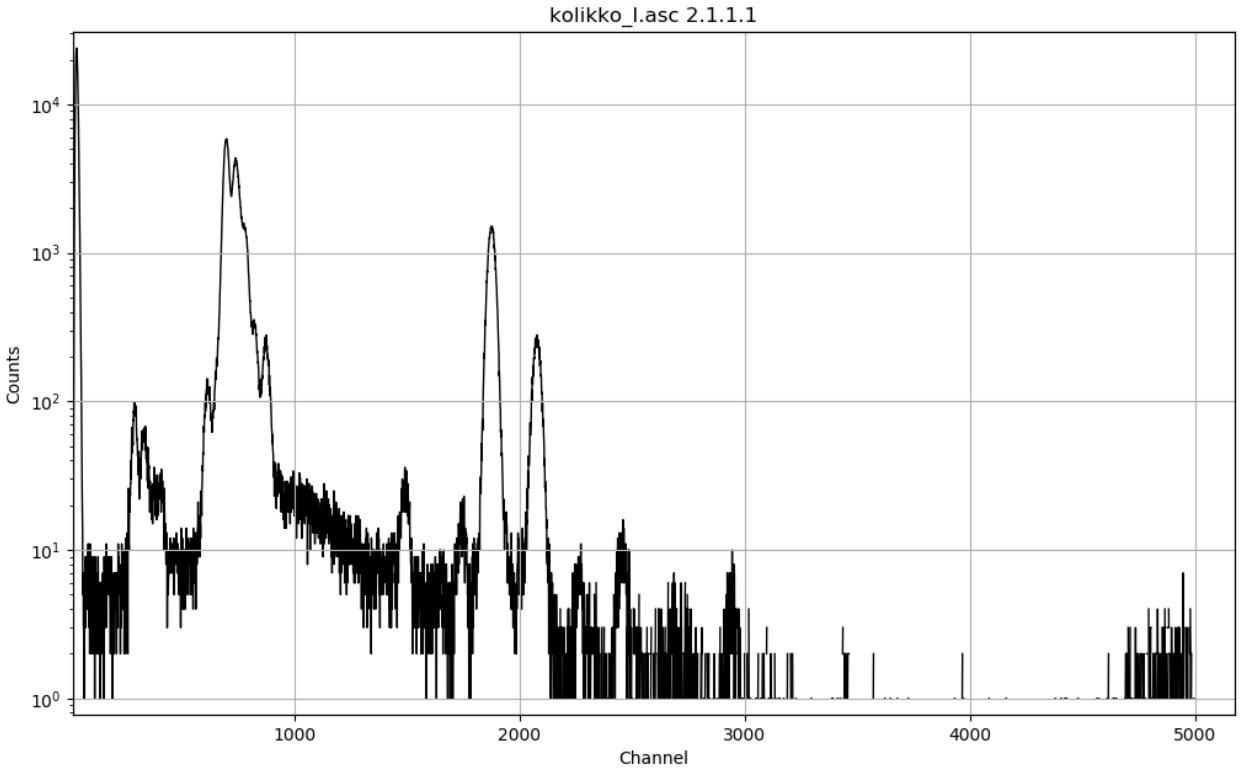

Appendix A.11: *Raw spectral data of coin I detected by SDD.*

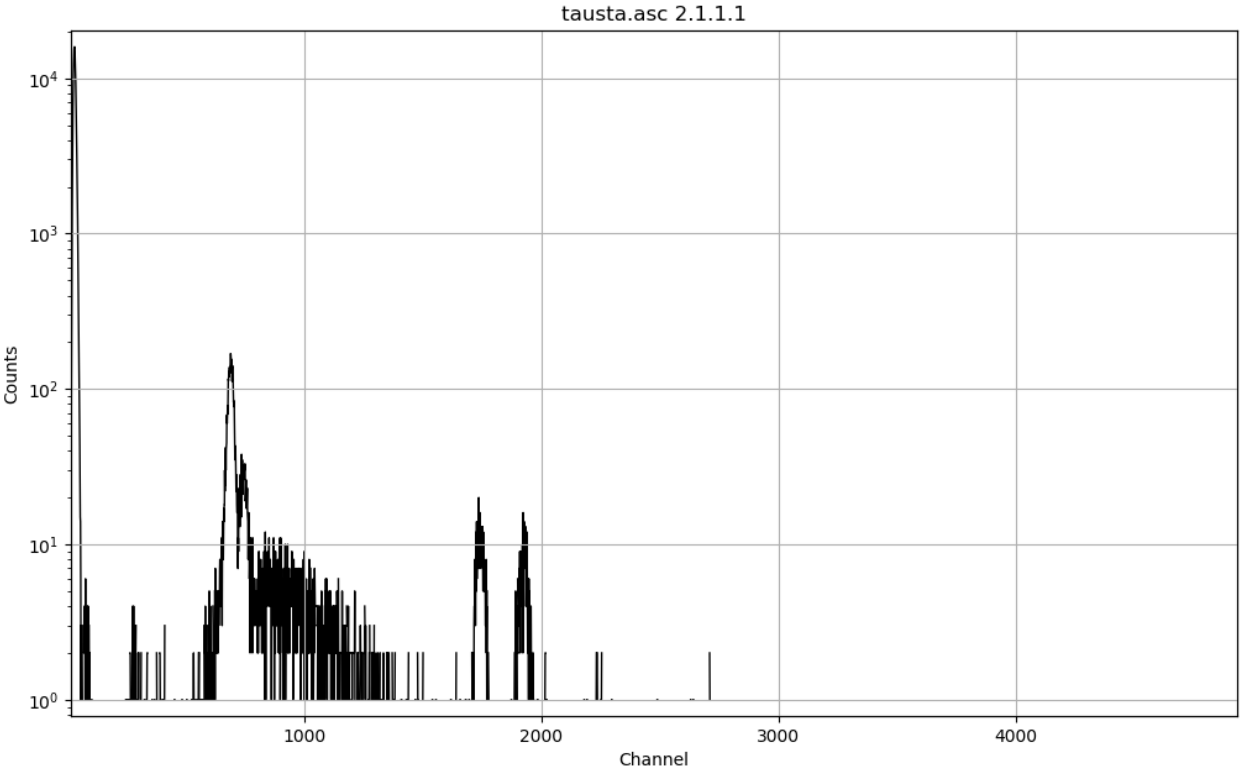

Appendix A.12: *Raw spectral data of background detected by SDD.*

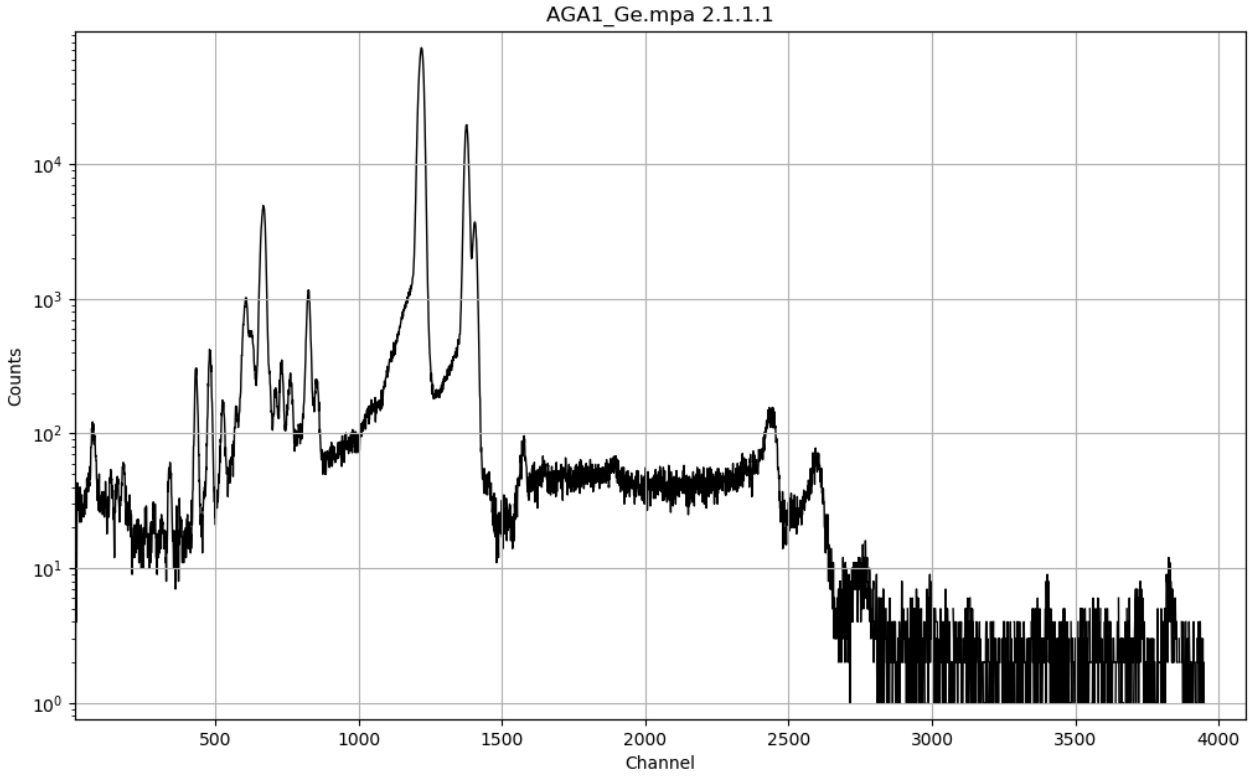

Appendix A.13: *Raw spectral data of reference material AGA1 by Ultra-LEGe detector.*

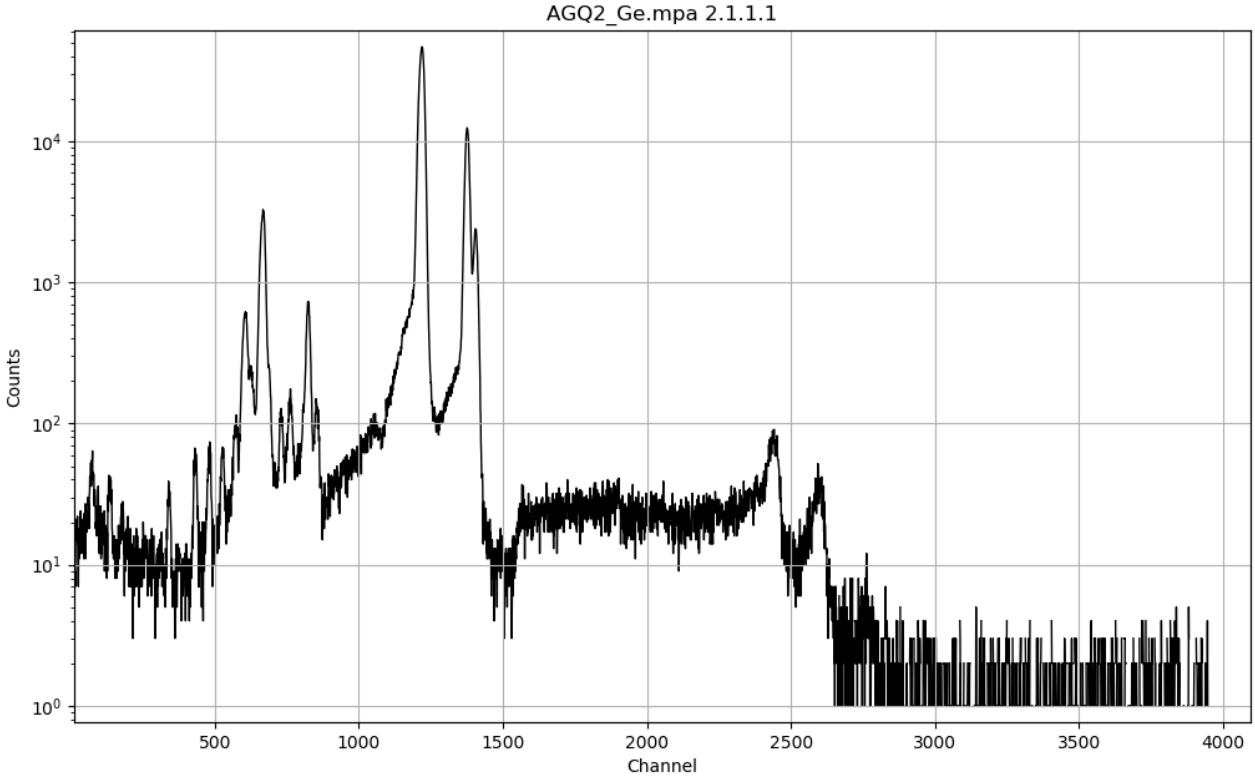

Appendix A.14: *Raw spectral data of reference material AGQ2 by Ultra-LEGe detector.*

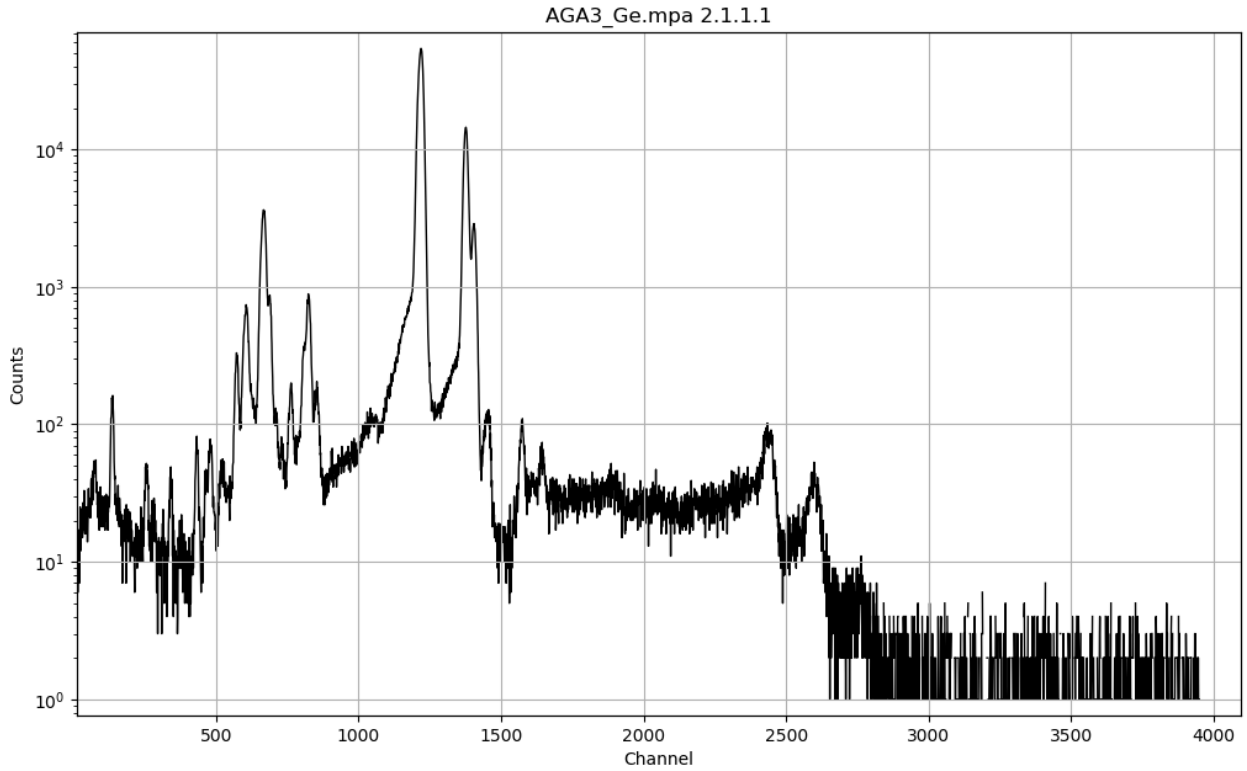

Appendix A.15: *Raw spectral data of reference material AGA3 by Ultra-LEGe detector.*

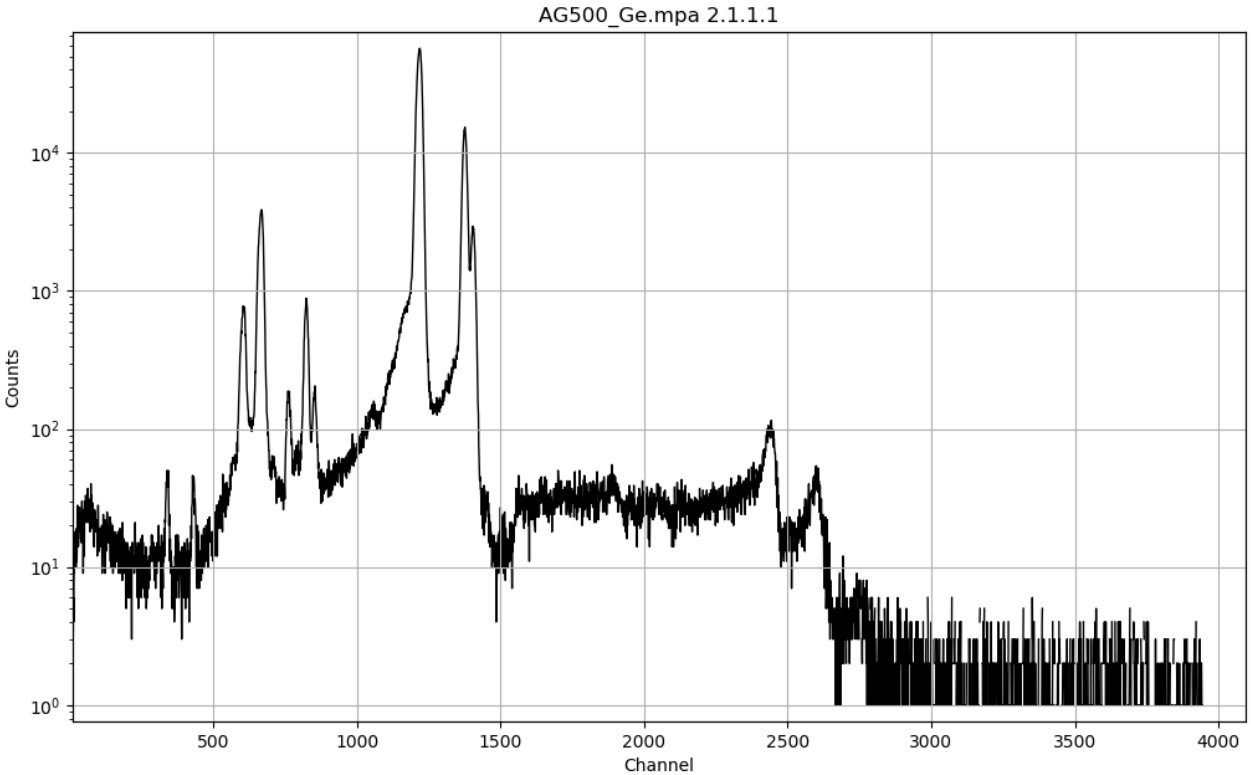

Appendix A.16: *Raw spectral data of reference material AG500 by Ultra-LEGe detector.*

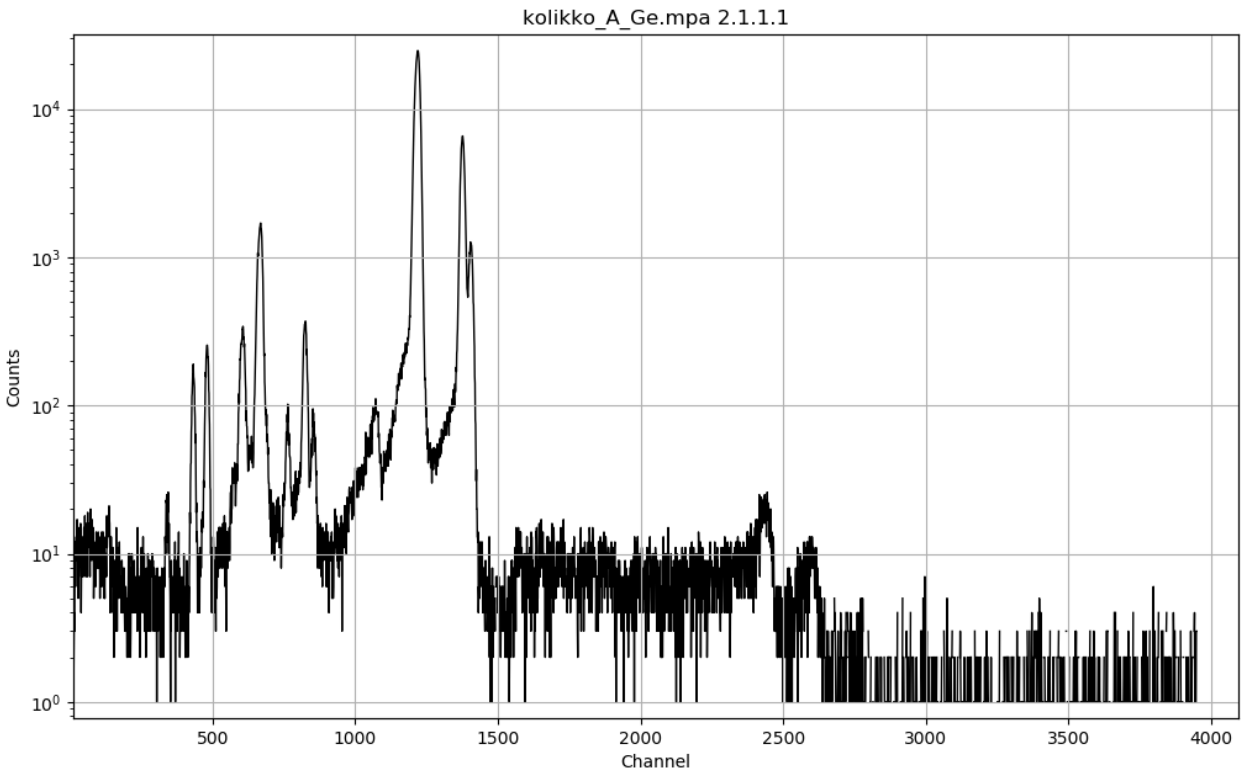

Appendix A.17: *Raw spectral data of coin A by Ultra-LEGe detector.*

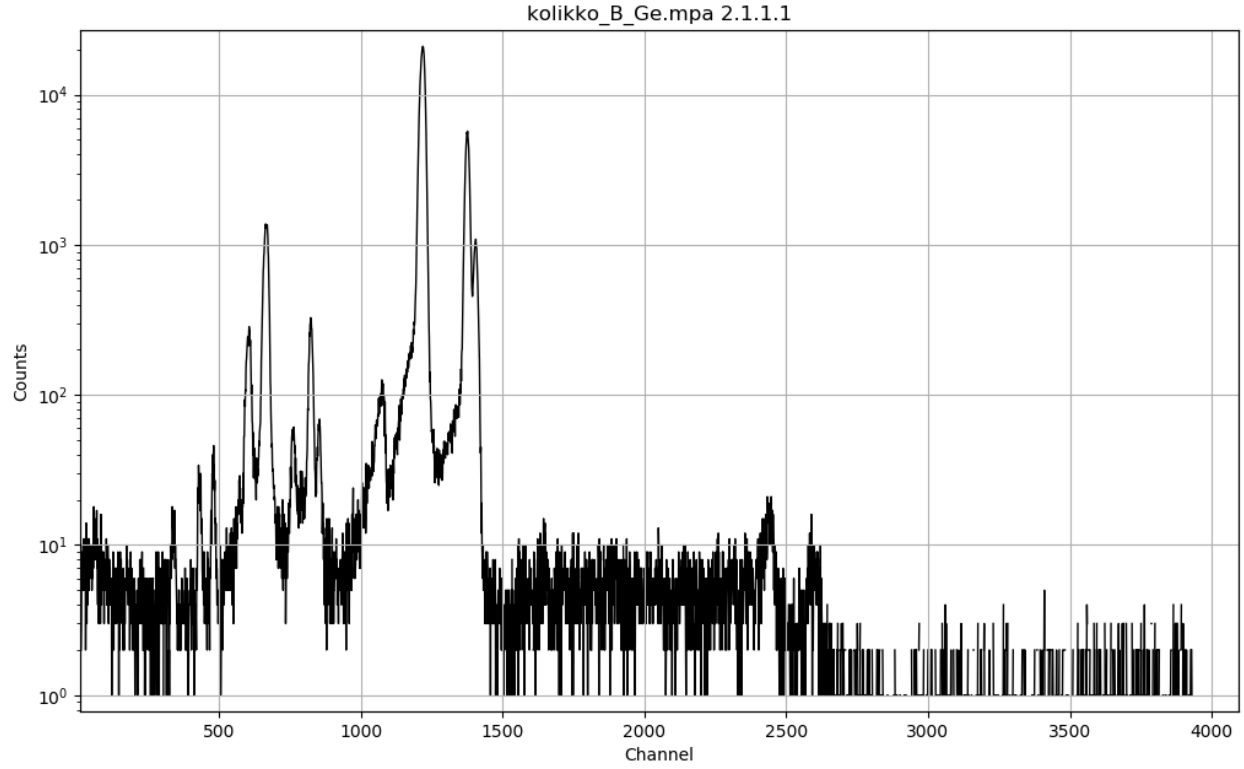

Appendix A.18: *Raw spectral data of coin B by Ultra-LEGe detector.*

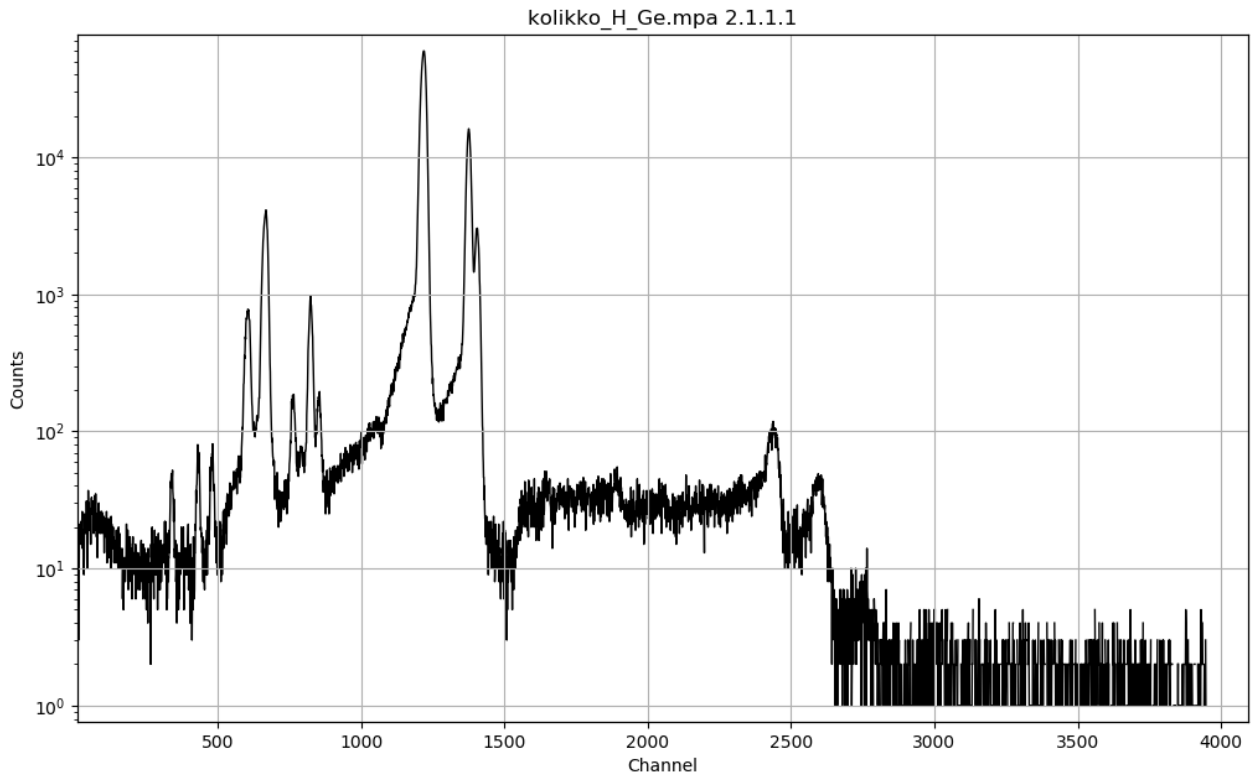

Appendix A.19: *Raw spectral data of coin H by Ultra-LEGe detector.*

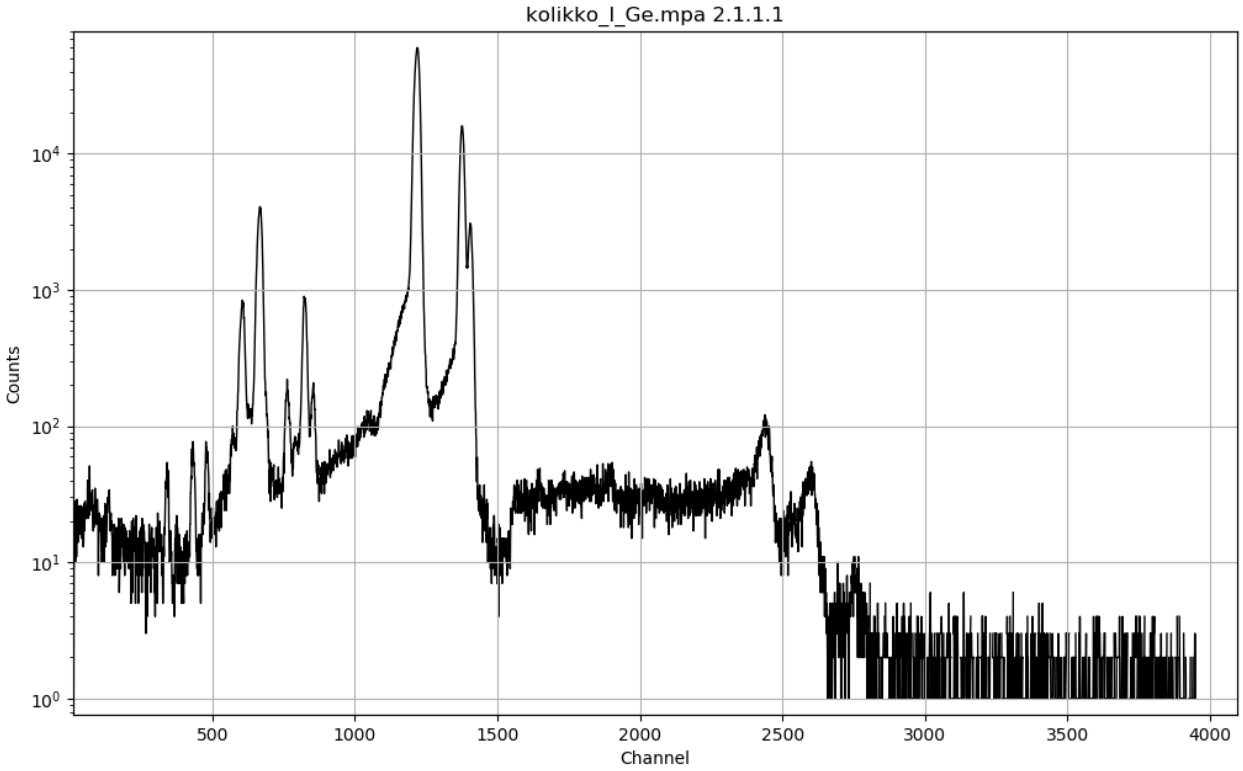

Appendix A.20: *Raw spectral data of coin I by Ultra-LEGe detector.*

Appendix B: Reference materials

Information of the reference materials used in the experiment is presented in appendices B.1 - B.4.

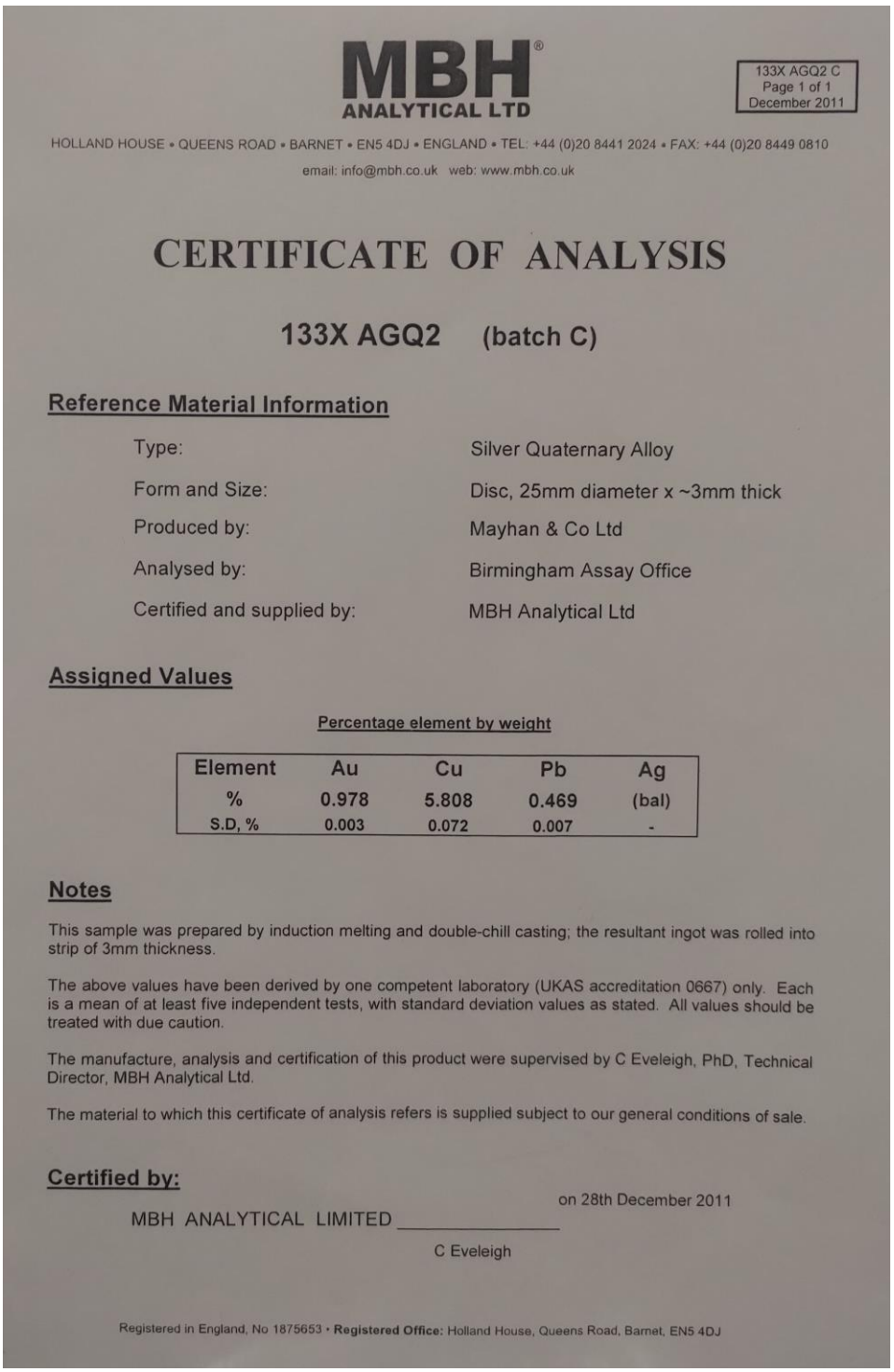

MBH®
ANALYTICAL LTD

133X AGQ2 C
Page 1 of 1
December 2011

HOLLAND HOUSE • QUEENS ROAD • BARNET • EN5 4DJ • ENGLAND • TEL: +44 (0)20 8441 2024 • FAX: +44 (0)20 8449 0810
email: info@mbh.co.uk web: www.mbh.co.uk

CERTIFICATE OF ANALYSIS

133X AGQ2 (batch C)

Reference Material Information

Type:	Silver Quaternary Alloy
Form and Size:	Disc, 25mm diameter x ~3mm thick
Produced by:	Mayhan & Co Ltd
Analysed by:	Birmingham Assay Office
Certified and supplied by:	MBH Analytical Ltd

Assigned Values

Percentage element by weight

Element	Au	Cu	Pb	Ag
%	0.978	5.808	0.469	(bal)
S.D, %	0.003	0.072	0.007	-

Notes

This sample was prepared by induction melting and double-chill casting; the resultant ingot was rolled into strip of 3mm thickness.

The above values have been derived by one competent laboratory (UKAS accreditation 0667) only. Each is a mean of at least five independent tests, with standard deviation values as stated. All values should be treated with due caution.

The manufacture, analysis and certification of this product were supervised by C Eveleigh, PhD, Technical Director, MBH Analytical Ltd.

The material to which this certificate of analysis refers is supplied subject to our general conditions of sale.

Certified by:

MBH ANALYTICAL LIMITED _____ on 28th December 2011

C Eveleigh

Registered in England, No 1875653 • **Registered Office:** Holland House, Queens Road, Barnet, EN5 4DJ

Appendix B.1: *Composition of the reference material AGQ2.*

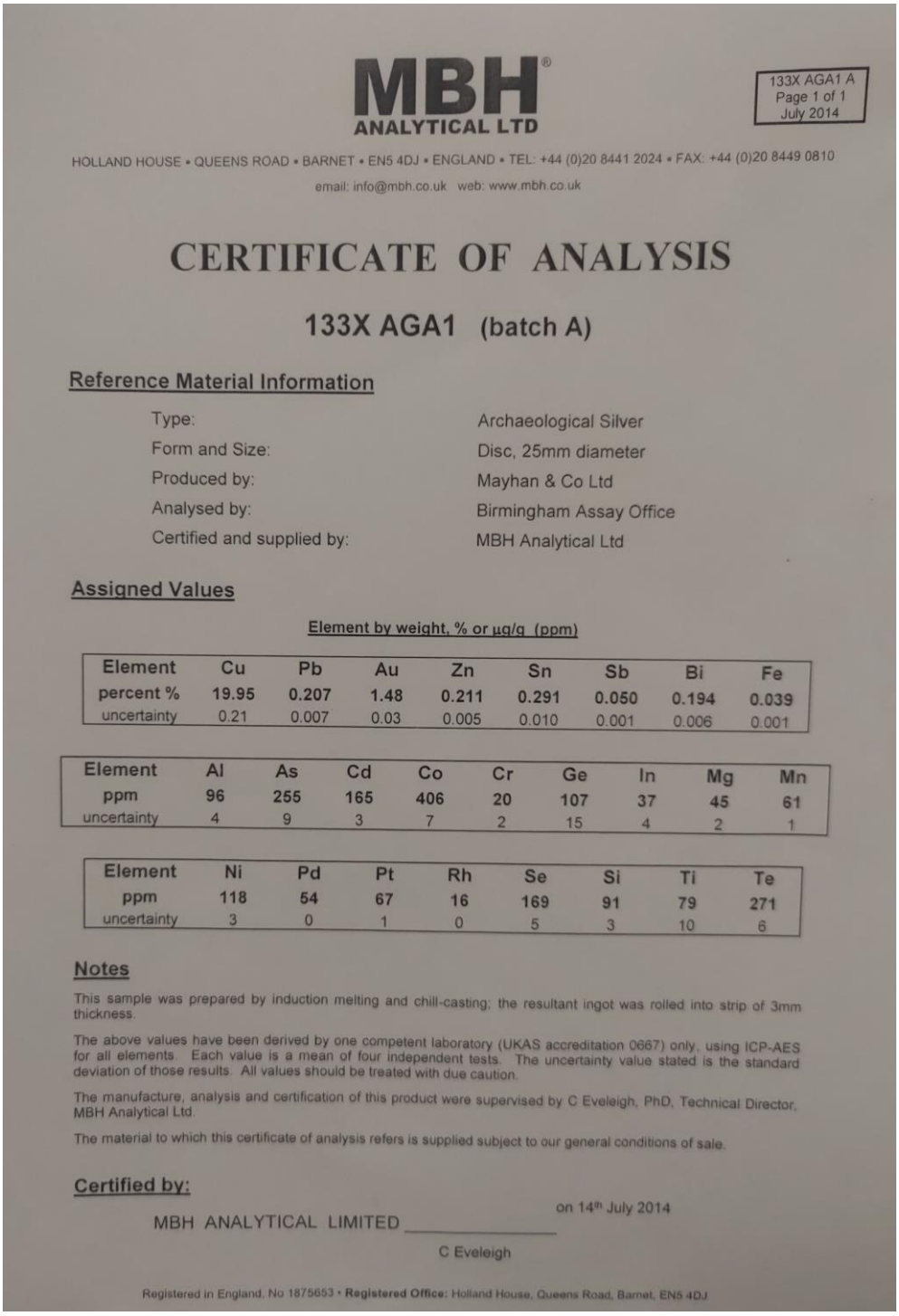

MBH®
ANALYTICAL LTD

133X AGA1 A
Page 1 of 1
July 2014

HOLLAND HOUSE • QUEENS ROAD • BARNET • EN5 4DJ • ENGLAND • TEL: +44 (0)20 8441 2024 • FAX: +44 (0)20 8449 0810
email: info@mbh.co.uk web: www.mbh.co.uk

CERTIFICATE OF ANALYSIS

133X AGA1 (batch A)

Reference Material Information

Type:	Archaeological Silver
Form and Size:	Disc, 25mm diameter
Produced by:	Mayhan & Co Ltd
Analysed by:	Birmingham Assay Office
Certified and supplied by:	MBH Analytical Ltd

Assigned Values

Element by weight, % or µg/g (ppm)

Element	Cu	Pb	Au	Zn	Sn	Sb	Bi	Fe
percent %	19.95	0.207	1.48	0.211	0.291	0.050	0.194	0.039
uncertainty	0.21	0.007	0.03	0.005	0.010	0.001	0.006	0.001

Element	Al	As	Cd	Co	Cr	Ge	In	Mg	Mn
ppm	96	255	165	406	20	107	37	45	61
uncertainty	4	9	3	7	2	15	4	2	1

Element	Ni	Pd	Pt	Rh	Se	Si	Ti	Te
ppm	118	54	67	16	169	91	79	271
uncertainty	3	0	1	0	5	3	10	6

Notes

This sample was prepared by induction melting and chill-casting; the resultant ingot was rolled into strip of 3mm thickness.

The above values have been derived by one competent laboratory (UKAS accreditation 0667) only, using ICP-AES for all elements. Each value is a mean of four independent tests. The uncertainty value stated is the standard deviation of those results. All values should be treated with due caution.

The manufacture, analysis and certification of this product were supervised by C Eveleigh, PhD, Technical Director, MBH Analytical Ltd.

The material to which this certificate of analysis refers is supplied subject to our general conditions of sale.

Certified by:

MBH ANALYTICAL LIMITED _____ on 14th July 2014

C Eveleigh

Registered in England, No 1875653 • **Registered Office:** Holland House, Queens Road, Barnet, EN5 4DJ

Appendix B.2: *Composition of the reference material AGA1.*

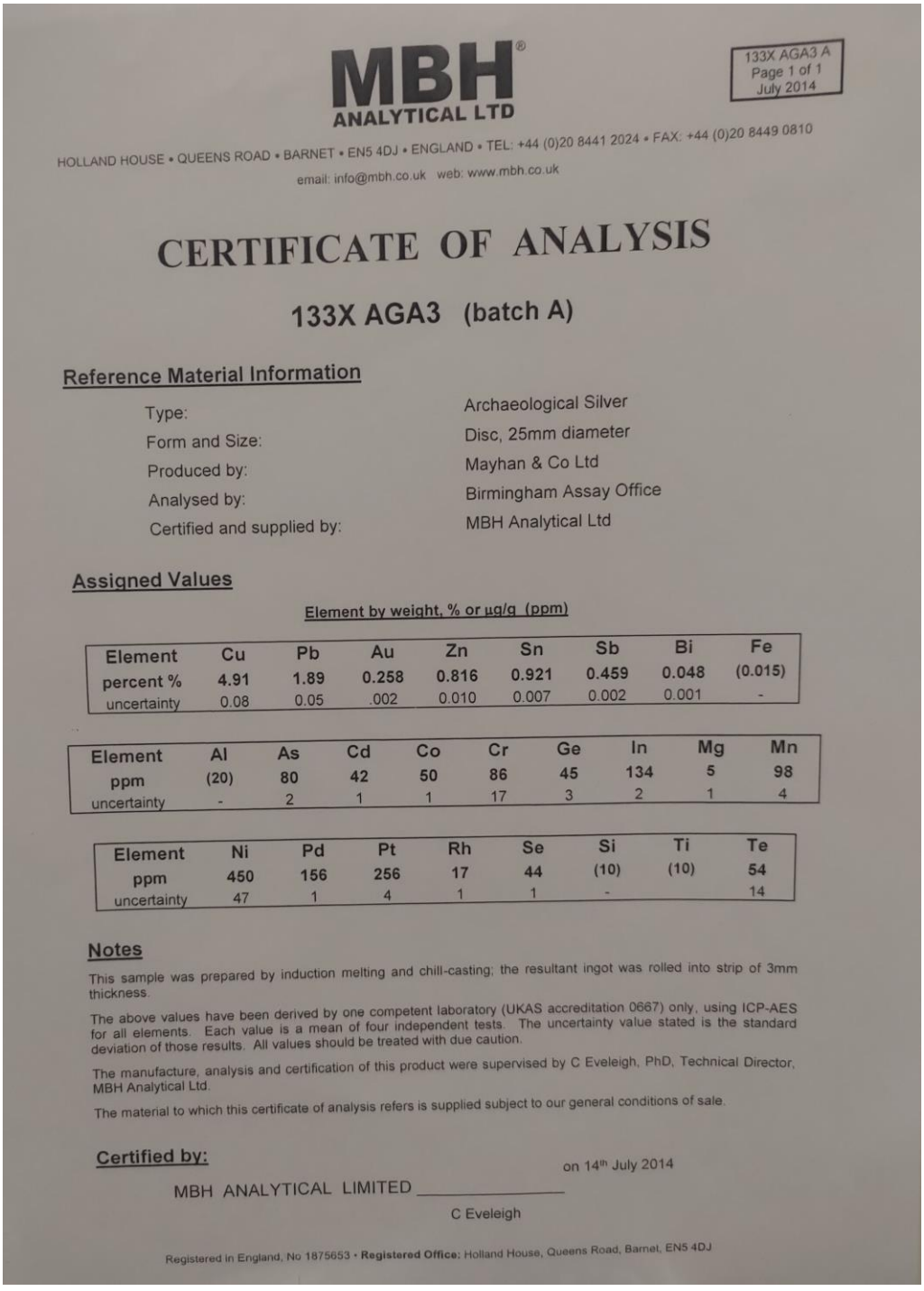

MBH®
ANALYTICAL LTD

133X AGA3 A
Page 1 of 1
July 2014

HOLLAND HOUSE • QUEENS ROAD • BARNET • EN5 4DJ • ENGLAND • TEL: +44 (0)20 8441 2024 • FAX: +44 (0)20 8449 0810
email: info@mbh.co.uk web: www.mbh.co.uk

CERTIFICATE OF ANALYSIS

133X AGA3 (batch A)

Reference Material Information

Type:	Archaeological Silver
Form and Size:	Disc, 25mm diameter
Produced by:	Mayhan & Co Ltd
Analysed by:	Birmingham Assay Office
Certified and supplied by:	MBH Analytical Ltd

Assigned Values

Element by weight, % or µg/g (ppm)

Element	Cu	Pb	Au	Zn	Sn	Sb	Bi	Fe
percent %	4.91	1.89	0.258	0.816	0.921	0.459	0.048	(0.015)
uncertainty	0.08	0.05	.002	0.010	0.007	0.002	0.001	-

Element	Al	As	Cd	Co	Cr	Ge	In	Mg	Mn
ppm	(20)	80	42	50	86	45	134	5	98
uncertainty	-	2	1	1	17	3	2	1	4

Element	Ni	Pd	Pt	Rh	Se	Si	Ti	Te
ppm	450	156	256	17	44	(10)	(10)	54
uncertainty	47	1	4	1	1	-		14

Notes

This sample was prepared by induction melting and chill-casting; the resultant ingot was rolled into strip of 3mm thickness.

The above values have been derived by one competent laboratory (UKAS accreditation 0667) only, using ICP-AES for all elements. Each value is a mean of four independent tests. The uncertainty value stated is the standard deviation of those results. All values should be treated with due caution.

The manufacture, analysis and certification of this product were supervised by C Eveleigh, PhD, Technical Director, MBH Analytical Ltd.

The material to which this certificate of analysis refers is supplied subject to our general conditions of sale.

Certified by:

on 14th July 2014

MBH ANALYTICAL LIMITED _____

C Eveleigh

Registered in England, No 1875653 • **Registered Office:** Holland House, Queens Road, Barnet, EN5 4DJ

Appendix B.3: *Composition of the reference material AGA3.*

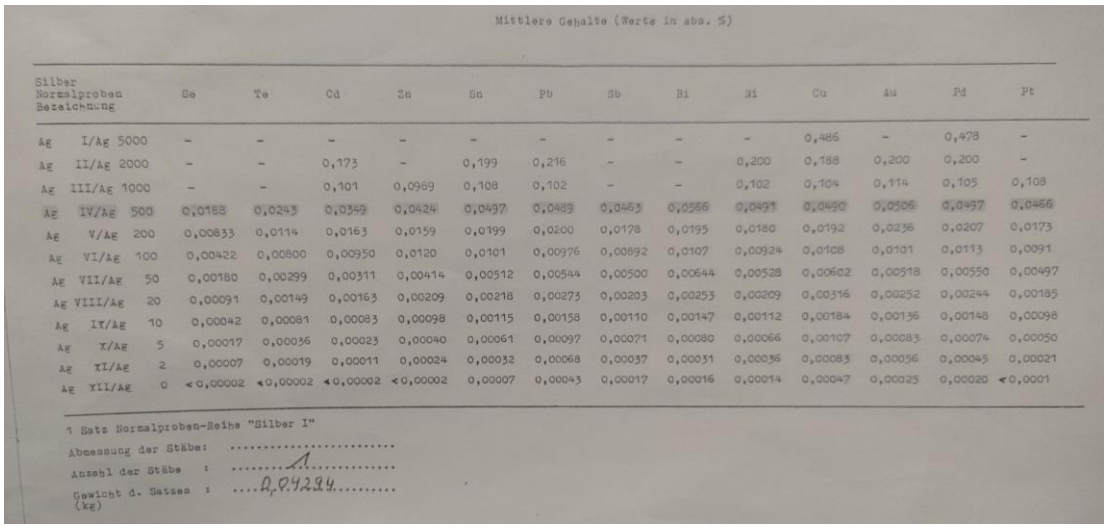

Mittlere Gehalte (Werte in abs. %)

Silber Normalproben Bezeichnung		Se	Te	Cd	Zn	Sn	Pb	Sb	Bi	Ni	Cu	Au	Pd	Pt
Ag	I/Ag 5000	-	-	-	-	-	-	-	-	-	0,486	-	0,478	-
Ag	II/Ag 2000	-	-	0,173	-	0,199	0,216	-	-	0,200	0,188	0,200	0,200	-
Ag	III/Ag 1000	-	-	0,101	0,0989	0,108	0,102	-	-	0,102	0,104	0,114	0,105	0,108
Ag	IV/Ag 500	0,0188	0,0243	0,0349	0,0424	0,0497	0,0489	0,0463	0,0556	0,0491	0,0490	0,0506	0,0497	0,0466
Ag	V/Ag 200	0,00833	0,0114	0,0163	0,0159	0,0199	0,0200	0,0178	0,0195	0,0180	0,0192	0,0236	0,0207	0,0173
Ag	VI/Ag 100	0,00422	0,00800	0,00950	0,0120	0,0101	0,00976	0,00892	0,0107	0,00924	0,0108	0,0101	0,0113	0,0091
Ag	VII/Ag 50	0,00180	0,00299	0,00311	0,00414	0,00512	0,00544	0,00500	0,00644	0,00528	0,00602	0,00518	0,00550	0,00497
Ag	VIII/Ag 20	0,00091	0,00149	0,00163	0,00209	0,00218	0,00273	0,00203	0,00253	0,00209	0,00316	0,00252	0,00244	0,00185
Ag	IX/Ag 10	0,00042	0,00081	0,00083	0,00098	0,00115	0,00158	0,00110	0,00147	0,00112	0,00184	0,00136	0,00148	0,00098
Ag	X/Ag 5	0,00017	0,00036	0,00023	0,00040	0,00061	0,00097	0,00071	0,00080	0,00066	0,00107	0,00083	0,00074	0,00050
Ag	XI/Ag 2	0,00007	0,00019	0,00011	0,00024	0,00032	0,00068	0,00037	0,00031	0,00036	0,00083	0,00056	0,00045	0,00021
Ag	XII/Ag 0	<0,00002	<0,00002	<0,00002	<0,00002	0,00007	0,00043	0,00017	0,00016	0,00014	0,00047	0,00025	0,00020	<0,0001

1 Satz Normalproben-Reihe "Silber I"

Abmessung der Stäbe: .....

Anzahl der Stäbe : .....1.....

Gewicht d. Satzes (kg) : ....0,04284.....

Appendix B.4: *Composition of the reference material AG500.*

Appendix C: Results

Silver coins (coins B, H, and I) detected by the SDD: Appendices C.1 - C.6.

Other coins (coins E and G) detected by the SDD: Appendices C.7 - C.10.

Silver coins (coins B, H, and I) detected by the Ultra-LEGe detector: Appendices C.11 - C.16.

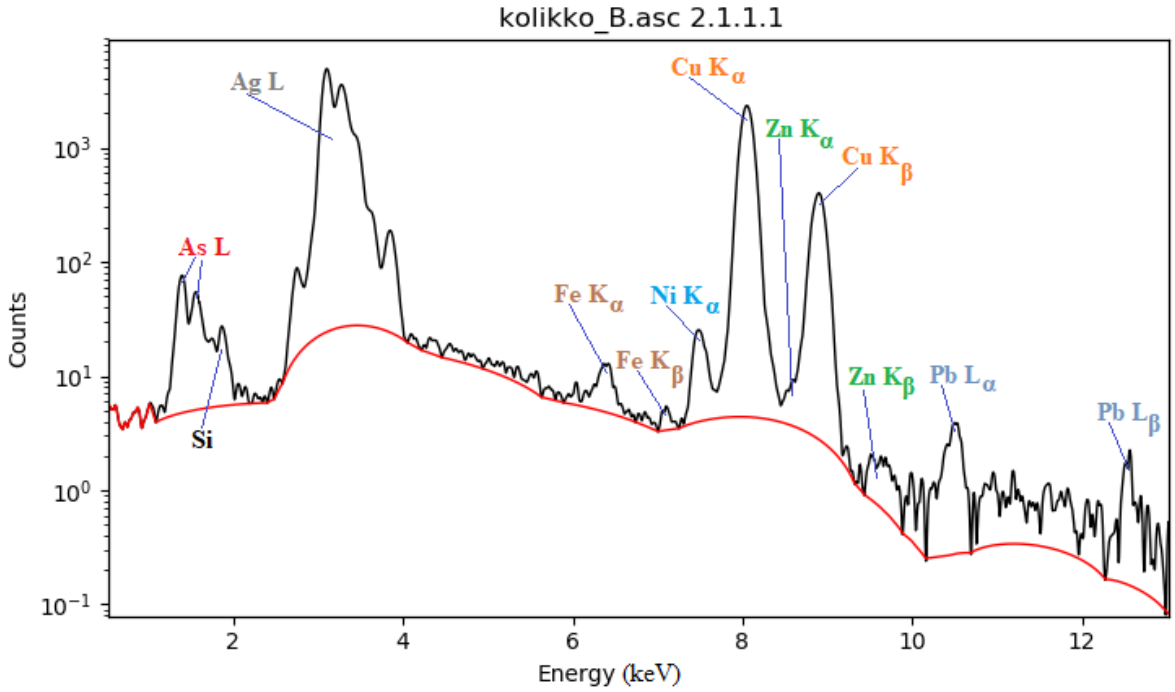

Appendix C.1: *PIXE spectrum of silver coin B detected by SDD.*

Element	X-ray emission line	Energy (keV)
As	L_3	1.282, 1.315
As	L_2	1.317, 1.350
As	L_1	1.380, 1.386, 1.485, 1.524
Ag	L_3	2.634, 2.978, 2.984, 3.256, 3.348
Ag	L_2	2.806, 3.151, 3.429, 3.520
Ag	L_1	3.203, 3.234, 3.433, 3.439, 3.743, 3.749
Fe	K_α	6.391, 6.404
Fe	K_β	7.058
Ni	K_α	7.461, 7.478
Cu	K_α	8.028, 8.048
Zn	K_α	8.616, 8.639
Cu	K_β	8.905
Zn	K_β	9.572
Pb	L_α	10.551
Pb	L_β	12.600

Appendix C.2: *Detected elements, lines, and possible x-ray energies in coin B.*

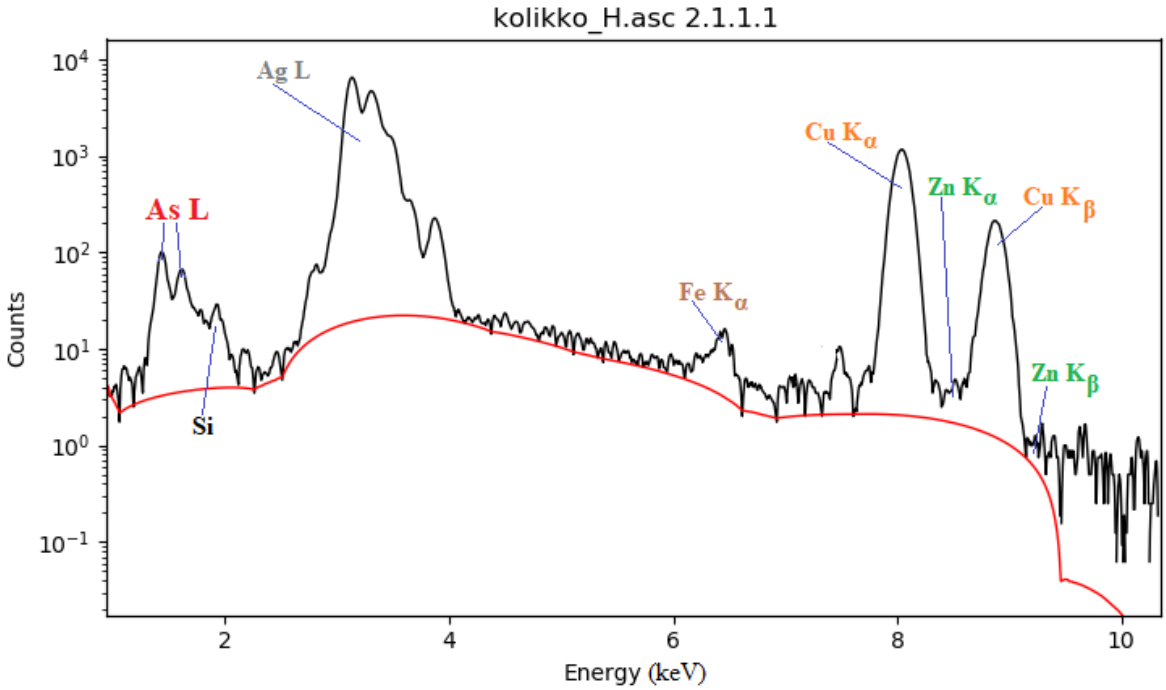

Appendix C.3: *PIXE spectrum of silver coin H detected by SDD.*

Element	X-ray emission line	Energy (keV)
As	L_3	1.282, 1.315
As	L_2	1.317, 1.350
As	L_1	1.380, 1.386, 1.485, 1.524
Ag	L_3	2.634, 2.978, 2.984, 3.256, 3.348
Ag	L_2	2.806, 3.151, 3.429, 3.520
Ag	L_1	3.203, 3.234, 3.433, 3.439, 3.743, 3.749
Fe	K_α	6.391, 6.404
Cu	K_α	8.028, 8.048
Zn	K_α	8.616, 8.639
Cu	K_β	8.905
Zn	K_β	9.572

Appendix C.4: *Detected elements, lines, and possible x-ray energies in coin H.*

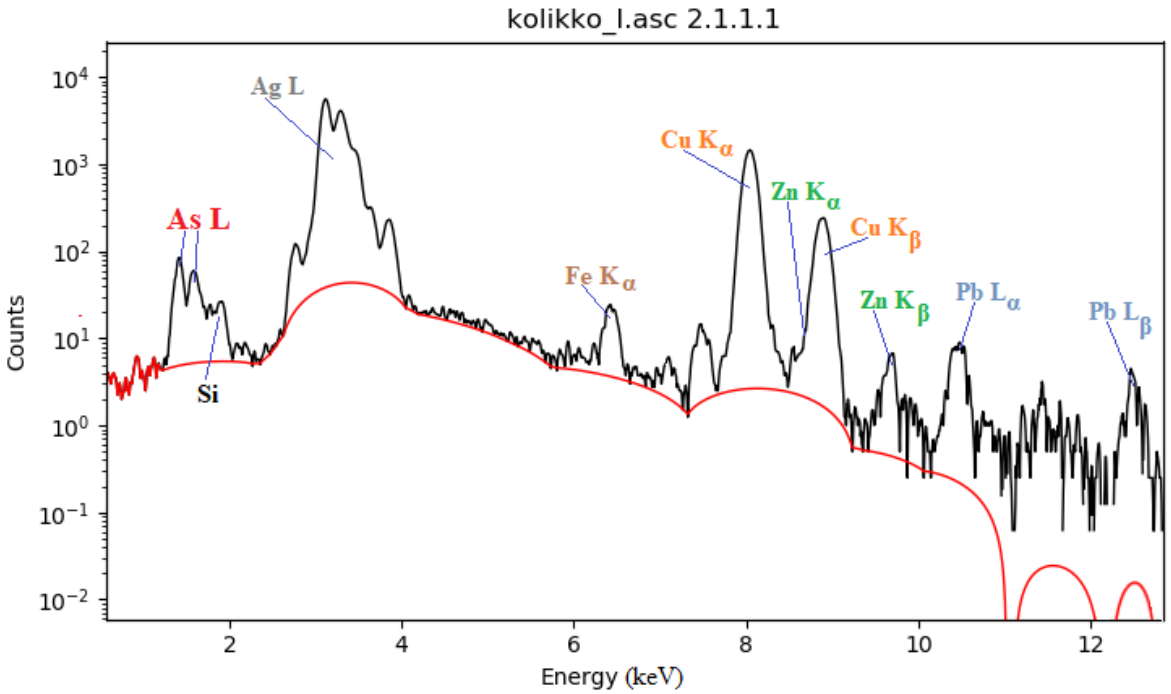

Appendix C.5: *PIXE spectrum of silver coin I detected by SDD.*

Element	X-ray emission line	Energy (keV)
As	L_3	1.282, 1.315
As	L_2	1.317, 1.350
As	L_1	1.380, 1.386, 1.485, 1.524
Ag	L_3	2.634, 2.978, 2.984, 3.256, 3.348
Ag	L_2	2.806, 3.151, 3.429, 3.520
Ag	L_1	3.203, 3.234, 3.433, 3.439, 3.743, 3.749
Fe	K_α	6.391, 6.404
Cu	K_α	8.028, 8.048
Zn	K_α	8.616, 8.639
Cu	K_β	8.905
Zn	K_β	9.572
Pb	L_α	10.551
Pb	L_β	12.600, 12.614, 12.622

Appendix C.6: *Detected elements, lines, and possible x-ray energies in coin I.*

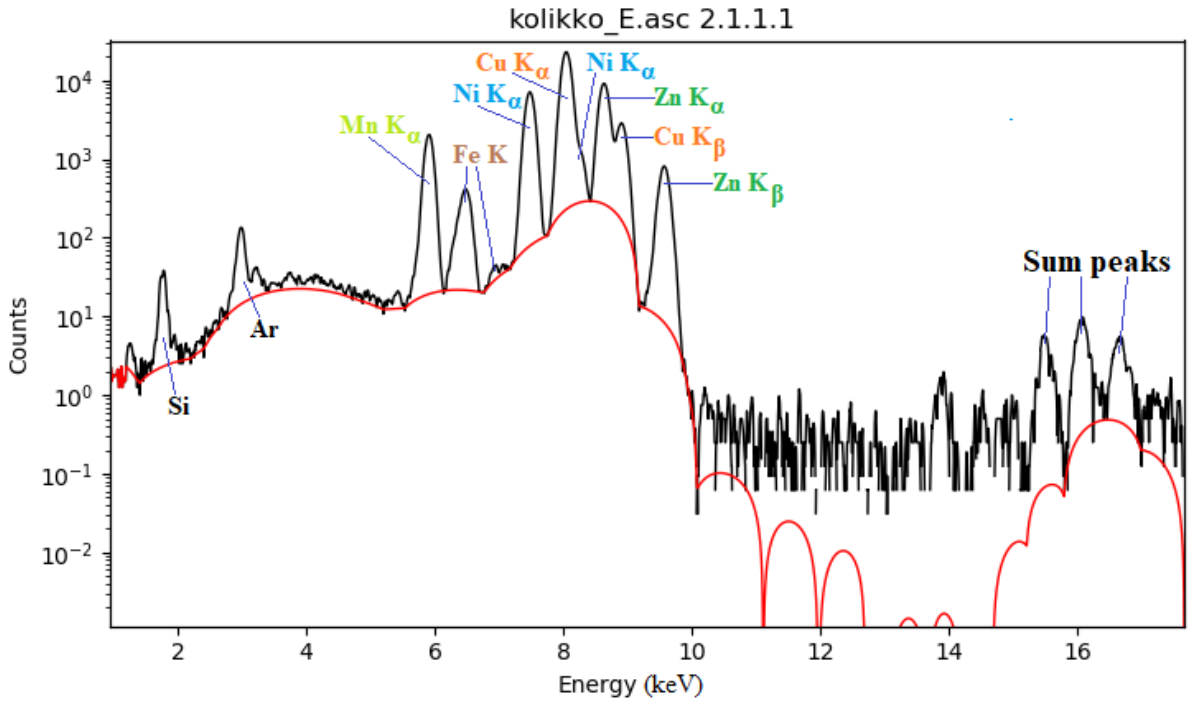

Appendix C.7: *PIXE spectrum of coin E detected by SDD.*

Element	X-ray emission line	Energy (keV)
Mn	K_α	5.888, 5.899
Fe	K_α	6.391, 6.404
Fe	K_β	7.058
Ni	K_α	7.461, 7.478
Cu	K_α	8.028, 8.048
Ni	K_β	8.265
Zn	K_α	8.616, 8.639
Cu	K_β	8.905
Zn	K_β	9.572

Appendix C.8: *Detected elements, lines, and possible x-ray energies in coin E.*

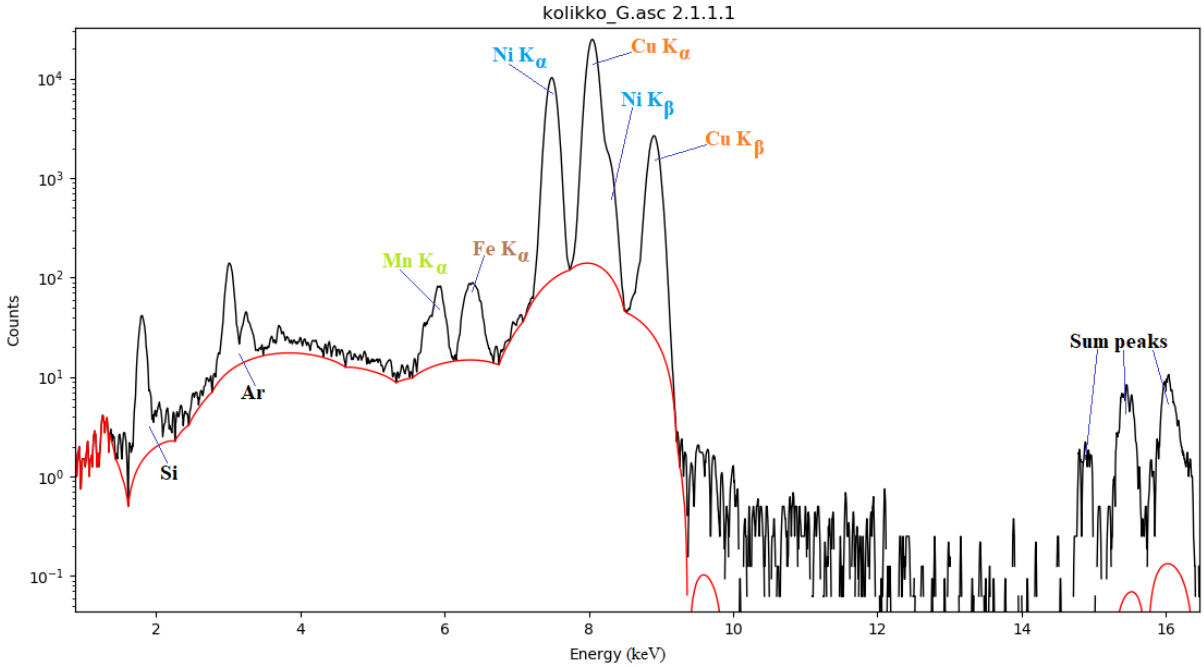

Appendix C.9: *PIXE spectrum of coin G detected by SDD.*

Element	X-ray emission line	Energy (keV)
Mn	K_α	5.888, 5.899
Fe	K_α	6.391, 6.404
Ni	K_α	7.461, 7.478
Cu	K_α	8.028, 8.048
Ni	K_β	8.265
Cu	K_β	8.905

Appendix C.10: *Detected elements, lines, and possible x-ray energies in coin G.*

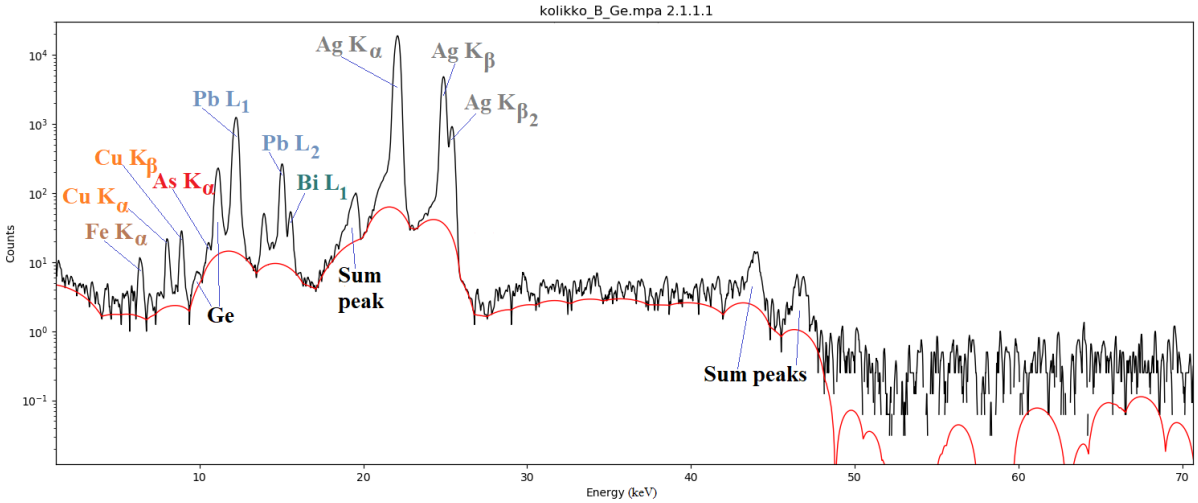

Appendix C.11: *PIXE spectrum of coin B detected by Ultra-LEGe detector.*

Element	X-ray emission line	Energy (keV)
Fe	K_α	6.391, 6.404
Cu	K_α	8.028, 8.048
Cu	K_β	8.905
As	K_α	10.544
Bi	L_2	11.712
Pb	L_1	12.307
Pb	L_2	15.503
Bi	L_1	15.582
Ag	K_α	21.990
Ag	K_β	24.912, 24.943
Ag	$K_{\beta 2}$	25.451, 25.458

Appendix C.12: *Detected elements, lines, and possible x-ray energies in coin B.*

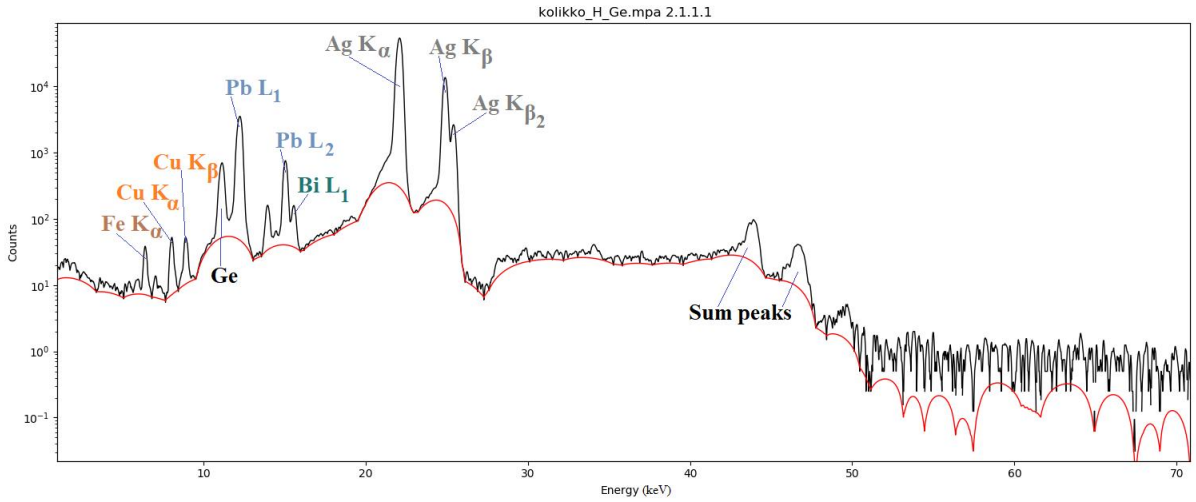

Appendix C.13: *PIXE spectrum of coin H detected by Ultra-LEGe detector.*

Element	X-ray emission line	Energy (keV)
Fe	K_α	6.391, 6.404
Cu	K_α	8.028, 8.048
Cu	K_β	8.905
Pb	L_1	12.307
Pb	L_2	15.503
Bi	L_1	15.582
Ag	K_α	21.990
Ag	K_β	24.912, 24.943
Ag	$K_{\beta 2}$	25.451, 25.458

Appendix C.14: *Detected elements, lines, and possible x-ray energies in coin H.*

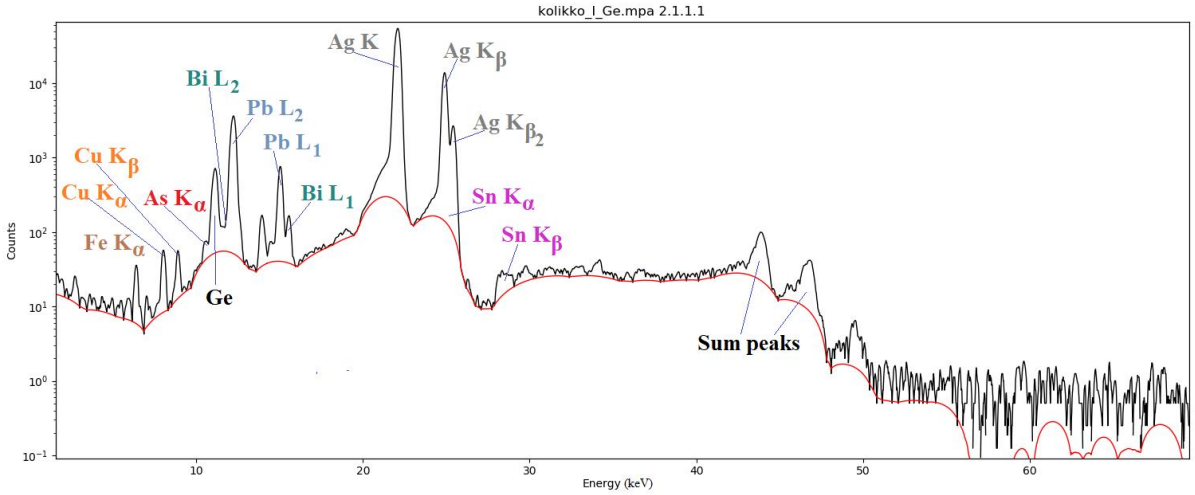

Appendix C.15: *PIXE spectrum of coin I detected by Ultra-LEGe detector.*

Element	X-ray emission line	Energy (keV)
Fe	K_α	6.391, 6.404
Cu	K_α	8.028, 8.048
Cu	K_β	8.905
As	K_α	10.544
Bi	L_2	11.712
Pb	L_1	12.307
Pb	L_2	15.503
Bi	L_1	15.582
Ag	K_α	21.990
Ag	K_β	24.912, 24.943
Sn	K_α	25.271
Ag	$K_{\beta 2}$	25.451, 25.458
Sn	K_β	28.444, 28.486

Appendix C.16: *Detected elements, lines, and possible x-ray energies in coin I.*